Department of Electrical Engineering and Automation

A Three-Phase to Single-Phase Midpoint Matrix Converter Using a Free-wheeling Switch for an Inductive Power Transfer System

Ferdi Perdana Kusumah

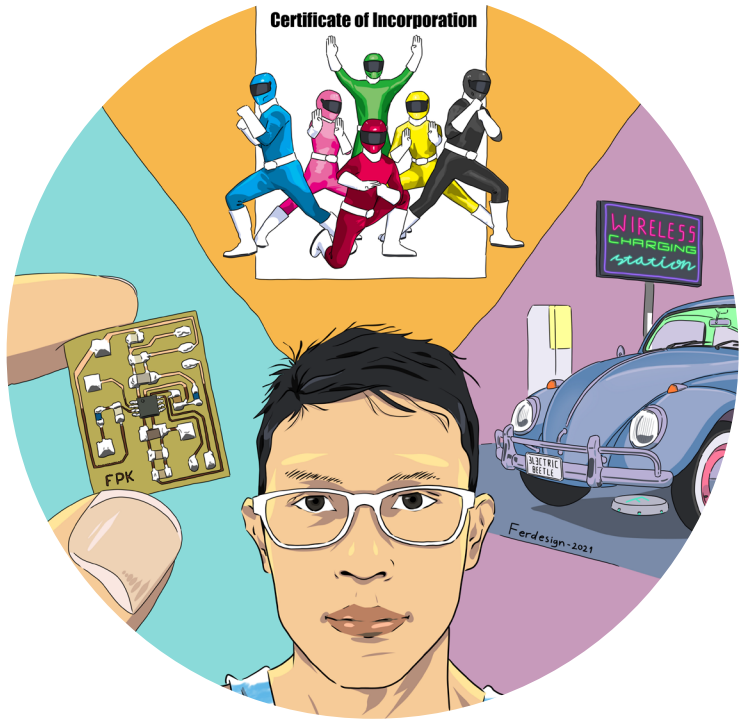

Aalto University

DOCTORAL DISSERTATIONS

Aalto University publication series
DOCTORAL DISSERTATIONS 99/2021

A Three-Phase to Single-Phase Midpoint Matrix Converter Using a Free-wheeling Switch for an Inductive Power Transfer System

Ferdi Perdana Kusumah

A doctoral dissertation completed for the degree of Doctor of Science (Technology) to be defended, with the permission of the Aalto University School of Electrical Engineering, at an online public examination (e.g. via Zoom) on 17 August 2021 at 12:15.

Aalto University
School of Electrical Engineering
Department of Electrical Engineering and Automation
Power Electronics

Supervising professor
Professor Jorma Kyyrä, Aalto University, Finland

Preliminary examiners
Professor Mahinda Vilathgamuwa, Queensland University of Technology (QUT), Australia
Associate Professor Kazuhiro Umetani, Okayama University, Japan

Opponent
Professor Omar Hegazy, Vrije Universiteit Brussel (VUB), Belgium

Aalto University publication series
DOCTORAL DISSERTATIONS 99/2021

ISBN 978-952-64-0453-0 (printed)
ISBN 978-952-64-0454-7 (pdf)
ISSN 1799-4934 (printed)
ISSN 1799-4942 (pdf)
http://urn.fi/URN:ISBN:978-952-64-0454-7

Images: Cover title: The Master Plan

Unigrafia Oy
Helsinki 2021

Finland

NORDIC SWAN ECOLABEL
Printed matter
4041-0619

Aalto University

Abstract

Aalto University, P.O. Box 11000, FI-00076 Aalto www.aalto.fi

Author
Ferdi Perdana Kusumah

Name of the doctoral dissertation
A Three-Phase to Single-Phase Midpoint Matrix Converter Using a Free-wheeling Switch for an Inductive Power Transfer System

Publisher School of Electrical Engineering

Unit Department of Electrical Engineering and Automation

Series Aalto University publication series DOCTORAL DISSERTATIONS 99/2021

Field of research Industrial Electronics and Electric Drives

Manuscript submitted 6 April 2021 **Date of the defence** 17 August 2021

Permission for public defence granted (date) 29 June 2021 **Language** English

☐ **Monograph** ☒ **Article dissertation** ☐ **Essay dissertation**

Abstract

Inductive power transfer (IPT) systems can improve the practicalities of a power delivery circuit. The contactless structure of IPT reduces the risk of sparking and electric shock, as well as provides good mobility for the IPT recipient during power transfer. Furthermore, the absence of moving parts on the transmitter and receiver circuits increases system reliability. The complexity of an IPT system that is connected to a three-phase voltage source can be reduced by utilizing a direct converter, such as a three-phase to single-phase Midpoint Matrix Converter using a Free-wheeling Switch (MMCFS). Additionally, the series-none compensation can also be applied in a high quality and coupling factors configuration. This dissertation explores the application of the MMCFS in a self-oscillating, series-none IPT system.

Two types of pulse-density modulation were proposed to run the converter: Non-successive Injection Modulation (NIM) and Successive Injection Modulation (SIM). Theoretical equations were formulated to estimate the characteristics of the MMCFS-based IPT (MMCFS-IPT) system. In addition, simulation models were created in PLECS to predict the IPT behavior in an ideal case. To validate the equations and the simulations, an experimental setup was designed and built for unidirectional power transfer. The setup consisted of programmable three-phase input voltage, the MMCFS, a primary compensation capacitor, a coupled inductor, a rectifier, and a resistive load. The converter used a field-programmable gate array to control a network of insulated-gate bipolar transistors. Experimental data were measured using a RCL meter, multimeters, oscilloscopes, and a thermal camera for further analysis.

In the case of unidirectional power transfer, SIM could produce three times the maximum output power compared to NIM using the same input voltage characteristics. Additionally, the current damping ratio, transfer efficiency and voltage gain depend on the series-none IPT coupling factor (k). The simulation results also confirmed that the proposed converter is capable of performing bi-directional power transfer using the series-series IPT configuration. In practice, applying NIM to MMCFS-IPT enables the converter to deliver as much power as 142 W to the resistive load based on a three-phase input amplitude of 70.8 V_{rms}. Power transfer can also be regulated through an on-off control system. The MMCFS-IPT prototype achieves an overall efficiency of around 80% based on a k of 0.53. The experimental results are in close agreement with both theoretical calculations and simulation results.

This research demonstrates that MMCFS can be used as an alternative to the rectifier-inverter topology in an IPT system in order to reduce system complexity, size and cost.

Keywords AC/AC converter, bi-directional power transfer, dynamic hysteresis comparator, inductive power transfer, matrix converter, on-off control, pulse-density modulation, wireless power transfer, zero-crossing detector, zero-current switching

ISBN (printed) 978-952-64-0453-0 **ISBN (pdf)** 978-952-64-0454-7

ISSN (printed) 1799-4934 **ISSN (pdf)** 1799-4942

Location of publisher Helsinki **Location of printing** Helsinki **Year** 2021

Pages 154 **urn** http://urn.fi/URN:ISBN:978-952-64-0454-7

Preface

This book is dedicated to my niece and nephew,
"Syakira Azkaina Sakhi" and "Raid Arka Safaraz", respectively.
I hope this work will inspire them to explore the wonderful world of science and technology.

(Me, lying on my apartment floor...) \[*_*]/

This dissertation is based on a research work conducted in the Department of Electrical Engineering and Automation, School of Electrical Engineering, Aalto University. The work was financially supported by Aalto university and Smart Otaniemi project. Additionally, the author also appreciates the encouragement grant from Walter Ahlström foundation.

First of all, I would like to give my gratitude to Prof. Jorma Kyyrä for accepting me as a doctoral student, and guiding me throughout my research work. I am very grateful for your trust and patient during the work, considering that I did not have a background in Power Electronics. I have learned a lot about the subject from you in the last 7 years. I would also like to thank Dr. Jussi Suomela, Prof. Emeritus Aarne Halme, Mr. Panu Sainio and Prof. Arto Visala. Thank you to Jussi for initially giving me an opportunity to be a doctoral student, and supervising me in your Generic Intelligent Machine team during my first year. Thank you to Aarne and Panu for giving me research work opportunities during Jussi's absence. And thank you to Arto for introducing me to Jorma when there was an uncertainty whether my research work could progress or not.

During the period of my research work, I received a lot of help from people working in the field of Power Electronics. The first version of experimental setup to be used in this dissertation was built by Mr. Simo Vuorsalo. He and Assistant Prof. Wilmar Martinez also gave useful advice regarding my research work as co-authors. In terms of practicality, Dr. Bahman Eskandari fixed phase detector in the experimental setup by lending his ADC-PLL circuit. Bahman also shared his experience with me in building a power electronics circuit. In addition, I also got a lot of support and help regarding teaching and research activities from other people in our research group: Dr. Elahe Doroudchi, Mr. Bilal Ahmad, Mr. Aniket Kulkarni, Dr. Prasad Jayathurathnage, Mr. Juha Mäkelä, Mr. Natan Baron-Trocellier, Mr. Yuvin Kokuhennadige and Ms. Liu Yining. Therefore, I would like to thank you for these invaluable contributions.

Thank you to Mr. Kenneth Pennington and Ms. Anya Siddiqi for checking the English grammar and textual clarity of this dissertation. And thank you to Prof. Mahinda Vilathgamuwa and Associate Prof. Kazuhiro Umetani for examining and giving critical feedbacks on this dissertation. Thank you to Prof. Omar Hegazy for agreeing to be an opponent. Thank you to all mathematicians who provided calculation methods used in this dissertation, and to all researchers who are cited in the reference section.

For administrative, purchasing and technical help related to my research, I would like to give my gratefulness to all the staffs of School of ELEC in Aalto University. Thank you to Ms. Leena Väisänen, Ms. Heidi Koponen, Ms. Jaana Hänninen, Ms. Essi Leinos, Ms. Riikka Mäkäräinen and Mr. Jari-Pekka Ruonio for helping me dealing with academic and travel documents, permits and other services. Thank you to Mr. Vesa Korhonen and Mr. Veli-Matti Niiranen, for helping me with project-related orders and PCB manufacturing process. Thank you to Mr. Ari Haavisto and Mr. Jouni Mäkinen for helping me building my experimental setup, and introducing me to laboratory equipments. I would also like to give my appreciations to other colleagues in the Department of Electrical Engineering and Automation for your assistance, help and friendship during my study years. Thank you to Ms. Zainab Saleem, Dr. Osama Mirza, Dr. Sergey Samokhin, Dr. Philipp Nguyen, Dr. Christian Giovanelli and Dr. Evgeny Nefedov, Mr. Harri Sapto Wijaya and Mr. Amir Sepehr. Thank you Aallonhuiput for organizing awesome social events! Thank you Aalto University!

I have been very lucky for having a lot of kind and caring friends whom I have met during my life in Finland. They are very inspiring, and I have learned invaluable things from them. Thank you to the Würzburg gang: Mr. Tobias Rudolf, Mr. Şenol Özkan, Ms. Hanka Bernardova and Dr. Jan Smíšek. Thank you to fellow Indonesian students: Ms. Margaretta Christita, Mr. Felix Abik, Mr. Amila Pramianshar, Mr. Prima Sanjaya, Mr. David Sibarani, Mr. Tito Adibaskoro, Ms. Zenith Purisha and the others that I cannot mention here. Thank you to Aalto-related people: Dr. Anja Thiede and Mr. Antonio Nikolov, Dr. Enrico and Ms. Anu Roverato, Mr. Dharma and Ms. Maria Srungavruksham, Dr. Mikhail and Ms. Daria Omelyanovich, Dr. José Luis Peralta, Dr. Benjamin Finley, Dr. Emilie Ressouche, Mr. Usama Tariq, Ms. Shikha Sharma, Ms. Evisa Collaku, Mr. Matti Sippola, Mr. Kha Nguyen, Ms. Caroline Moinel, Ms. Noemi Valero, Ms. Helena Meissner, Mr. Soumya Hazra, Mr. Sebastian Verho and Ms. Salla Hossi. And thank you to the rest I have met during my life in Finland: Mr. Jan Lukac, Mr. Sina Bahrpeyma, Ms. Mariel Hynynen, Ms. Anna vd Velde, Ms. Sara-Sofia Sahlman, Ms. Afeera Mirza, Ms. Silja Hyyrynen, Ms. Henrietta Nyström, Ms. Asuka Kanai, Ms. Ninja Tukiainen, Ms. Anja Sivonen, Mr. Juha Penttinen, Mr. Arkadiusz Hiler, Mr. Jorge Sinisterra, Ms. Verna

Wahlbom, Mr. Kim Parviainen and Ms. Patrycja Dittmann-Wałach. Thank you all for organizing awesome parties and hangouts, board-game events, culinary expeditions, hiking and camping, hearing my personal problems, as well as giving me advices in general. My life experience in Finland would be different without you. Unfortunately, it is not possible to list all people I know during my study years. So, to all of you who have not been mentioned, thank you for being a part of my life! Thank you Finland!

During my research and study periods, I mainly involved in two different student associations, where I learned about responsibilities and time management. Thank you to PPI Finlandia ry. and all its members for giving me a platform to organize Indonesian student events, and giving me networking opportunities with government officials in Finland. Thank you to the people who supported me during my period of activity in the association: Dr. Windi Indra Muziasari, Dr. Imam Santoso, Mr. Achmad Maulana, Dr. Dyah Listyarifah, Dr. Mukrimin, Mr. Arif Tirto Aji, Ms. Dinda Fadhila, Ms. Indri Wulandari, Ms. Carmelita Ginting-Carlström , Ms. Bernadetta Ginting-Szczesny and Dr. Adrianto Dwi Nugroho. Thank you to Äänenkannattajat ry. and all its members for giving me an opportunity to sing, and to organize choir practices and concerts. Thank you for the currently active board members: Mr. Juhana Mäntymaa, Ms. Tone Knapstad, Ms. Lauren Jung, Dr. Matteo Pozza, Dr. Karol Schober and Ms. Essi Toivonen. Additionally, thank you to Aalto Breakers crew: Mr. Juho Seppänen, Mr. Hai Phan, Ms. Rosa-Maria Alaraasakka, Mr. Henry Leskinen, Mr. Anton Sutinen and Mr. Aleksi Miettinen, for organizing bboy practices and shows.

Finally, I would like to thank my family, who has given me support and encouragement to finish this research work. To my parents, Mr. Yayan Sutaryan and Ms. Cicih Sunarsih, as well as my sister Ms. Ferni Erdina, I always love you despite our different perspective in seeing the world.

Terima kasih buat bapak, ibu, sama ade atas dukungan yang telah diberikan selama ini, baik berupa materi maupun moral. Semoga disertasi ini bisa menginspirasi dan memberikan manfaat bagi banyak orang.

Cautionary advice: In order to understand all topics given in this book, the reader is recommended to have basic knowledge of linear algebra, calculus, electric circuit, and power electronics.

Helsinki, July 20, 2021,

Ferdi Perdana Kusumah

BVZZTRSEP8Q65AEWCG8L66QCDYEDMTHZWBZOC2S106EAWXX344AVDKJ3N99
APSBB3A675VTXAOJGTAJMZKBGCA2H2RGPUP3X7OBUCG6Q97GBQCA54S17
MRQTQHOMJCYPQBVUBRHCRNTYBZK

Contents

List of Publications

This doctoral dissertation presents an overview of the following six publications which are referred to in the text by their Roman numerals:

I Ferdi Perdana Kusumah and Jorma Kyyrä. Minimizing Coil Power Loss in A Direct AC/AC Converter-Based Contactless Electric Vehicle Charger. In *2017 19th European Conference on Power Electronics and Applications (EPE'17 ECCE Europe)*, 10 pages, Warsaw, Poland, Sep. 2017.

II Ferdi Perdana Kusumah and Jorma Kyyrä. A Zero-Crossing Approximation of a Distorted Sinusoidal Signal Using Analog Circuit. In *43rd Annual Conference of the IEEE Industrial Electronics Society (IECON 2017)*, 6 pages, Beijing, China, Oct. 2017.

III Ferdi Perdana Kusumah and Jorma Kyyrä. Initial Current Injection Method of A Direct Three-Phase to Single-Phase AC/AC Converter for Inductive Charger. In *2018 International Power Electronics Conference (IPEC-Niigata 2018 ECCE Asia)*, 7 pages, Niigata, Japan, May 2018.

IV Ferdi Perdana Kusumah and Jorma Kyyrä. Bi-directional Power Transfer of a Contactless Electric Vehicle Charger Using Direct Three-Phase to Single-Phase AC/AC Converter. In *2018 20th European Conference on Power Electronics and Applications (EPE'18 ECCE Europe)*, 10 pages, Riga, Latvia, Sep. 2018.

V Ferdi Perdana Kusumah and Jorma Kyyrä. Successive injections modulation of a direct three-phase to single-phase AC/AC converter for a contactless electric vehicle charger. *The Journal of Engineering*, Volume 2019, Issue 17, pp. 4106-4110, Jan. 2019.

VI Ferdi Perdana Kusumah, Jorma Kyyrä and Wilmar Martinez. A Self-Oscillating Series-None Inductive Power Transfer System Using A Matrix Converter. Submitted to *IEEE Transaction on Power Electronics*, 10 pages, April 2021.

Author's Contribution

Publication I: "Minimizing Coil Power Loss in A Direct AC/AC Converter-Based Contactless Electric Vehicle Charger"

The author built the MMCFS topology and its modulation strategy by following the advice and insight of the co-author. The MMCFS structure is based on a single-phase to single-phase direct AC/AC converter. The topic was proposed by the author to improve the efficiency of a series-none inductive power transfer system using MMCFS. A steady-state mathematical model and its recursive solution were developed by the author to quantify and predict system behavior. Furthermore, the author also built a computer simulation to validate the model. The paper was written by the author, while the co-author contributed advice, as well as manuscript checking and correction.

Publication II: "A Zero-Crossing Approximation of a Distorted Sinusoidal Signal Using Analog Circuit"

The circuit and the idea were proposed by the author. A mathematical model was derived by the author, and theoretical calculations were performed based on this model. To validate the model, a computer simulation was also built by the author. The paper was written by the author, while the co-author contributed advice, as well as manuscript checking and correction.

Publication III: "Initial Current Injection Method of A Direct Three-Phase to Single-Phase AC/AC Converter for Inductive Charger"

The author proposed the topic that is inspired by the DC resonant charging

circuit. Dynamic and steady-state mathematical models, as well as theoretical results were developed and calculated by the author. The author also built a computer simulation to validate the models. The paper was written by the author, while the co-author contributed advice, as well as manuscript checking and correction.

Publication IV: "Bi-directional Power Transfer of a Contactless Electric Vehicle Charger Using Direct Three-Phase to Single-Phase AC/AC Converter"

The idea of bi-directional power transfer came from the co-author and was further developed by the author. The development and calculations of the steady-state theoretical model were conducted by the author. The author also built a computer simulation to support the model and analyzed its waveforms and numerical values. The paper was written by the author, while the co-author contributed advice, as well as manuscript checking and correction.

Publication V: "Successive injections modulation of a direct three-phase to single-phase AC/AC converter for a contactless electric vehicle charger"

The proposed modulation is inspired by the line-to-line commutation of inverter. The author constructed a steady-state mathematical model and performed theoretical calculations to predict the MMCFS behavior. In addition, a computer simulation was constructed to validate the calculations. The paper was written by the author, while the co-author contributed advice, as well as manuscript checking and correction.

Publication VI: "A Self-Oscillating Series-None Inductive Power Transfer System Using A Matrix Converter"

The author proposed the topology, modulation strategy and experimental setup of MMCFS-IPT. The setup was designed, partially built, and tested by the author. Mathematical model formulation, computer simulation construction, and theoretical calculations were done by the author. Additionally, practical behavior of the IPT system to validate the mathematical model were performed by the author. The paper was written by the author, while the co-authors contributed advice, as well as manuscript checking and correction.

List of Figures

List of Tables

Abbreviations

AC	Alternating current
DC	Direct current
DHC	Dynamic Hysteresis Comparator
FPGA	Field-programmable gate array
FWO	Free-Wheeling Oscillation
IGBT	Insulated-gate bipolar transistor
IPT	Inductive Power Transfer
LC	Inductor-capacitor circuit
LC-L	A network of capacitor and coupled inductor
MMCFS	Midpoint Matrix Converter using a Free-Wheeling Switch
MMCFS-IPT	MMCFS-based IPT
NIM	Non-successive Injection Modulation
PCB	Printed circuit board
PDM	Pulse-density modulation
PTS	Primary to Secondary
PWM	Pulse-width modulation
RCL	A network of resistor, capacitor, and inductor
RI	Rectifier-Inverter
RMS	Root mean square
SIM	Successive Injection Modulation

STP	Secondary to Primary
VB2B	Voltage Back-to-Back
ZCD	Zero-crossing detector
ZCS	Zero-current switching

Symbols

Latin letter symbols:

$\mathbf{A}$	State matrix
C	Capacitor
C_{DC}	The intermediate capacitor of VB2B
C_{d}	Differentiator capacitor
C_{f}	Filter capacitor
C_{L}	Smoothing capacitor
C_{p}	Primary compensation capacitor
C_{s}	Secondary compensation capacitor
c_3	Real constant
D	Discriminant
d_{c}	Coil separation distance
d_{i}	Inner coil diameter
d_{o}	Outer coil diameter
d_{s}	The wire separation distance of a coil
$\mathrm{d}t$	The differential of t
d_{w}	The wire diameter of a coil
f_{l}	Line voltage frequency in Hertz
f_0	Resonant frequency in Hertz
G	Voltage gain

I_{lim}	Current amplitude limit
I_{p}	The amplitude of i_{p}
I_{ref}	Current amplitude reference
I_{s}	The amplitude of i_{s}
i_{m}	Inductance measurement current
i_{p}	The current of MMCFS
$\hat{i}_{\mathrm{p}}$	The peak current of i_{p}
$i_{\mathrm{p(res)}}$	The primary resonant current of MMCFS-IPT
i_{s}	The secondary-side current of MMCFS-IPT
$\hat{i}_{\mathrm{s}}$	The peak current of i_{s}
$i_{\mathrm{s(res)}}$	The secondary resonant current of MMCFS-IPT
j	Imaginary number
k	Coupling factor
k_0, k_1	Summation index
L	Inductor
L_1	Series-connected inductance (opposite polarity)
L_2	Series-connected inductance (identical polarity)
L_{p}	Primary coil inductance
L_{s}	Secondary coil inductance
M	Mutual inductance
Max	Maximum absolute value operator
Min	Minimum absolute value operator
N_0, N_1, N_2	The lower/upper bound of a summation
N_{t}	The number of turns in a coil
n	Multiplication constant
P_{nim}	The primary-side power of NIM
P_{p}	The average power of MMCFS
P_{s}	The secondary-side average power of MMCFS-IPT

P_{sim}	The primary-side power of SIM
P_{sqr}	The equivalent average power of P_{p}
Q_{p}	Primary coil quality factor
Q_{s}	Secondary coil quality factor
R	Resistor
R_{d}	Differentiator resistor
R_{eq}	Equivalent AC resistive load
R_{f}	Filter resistor
R_{g}	Gate resistance
R_{L}	Resistive load
R_{opt}	The optimum value of R_{eq}
R_{p}	Primary coil resistance
R_{s}	Secondary coil resistance
$\mathrm{S_{an}}$, $\mathrm{S_{bn}}$, $\mathrm{S_{cn}}$, $\mathrm{S_{dn}}$,	
$\mathrm{S_{ap}}$, $\mathrm{S_{bp}}$, $\mathrm{S_{cp}}$, $\mathrm{S_{dp}}$,	
$\mathrm{S_{f1}}$, $\mathrm{S_{f2}}$, $\mathrm{S_{g1}}$, $\mathrm{S_{g2}}$	IGBT with its own anti-parallel diode
s, s_1, s_2, s_3	Complex number
s_{an}, s_{bn}, s_{cn}, s_{dn},	
s_{ap}, s_{bp}, s_{cp}, s_{dp},	
s_{f1}, s_{f2}, s_{g1}, s_{g2}	IGBT gate driver signal
sin	Sinusoidal function
T_0	Resonant frequency period
T_{asc}	The ascending duration of multistep switching
T_{des}	The descending duration of multistep switching
T_{b}	Switch blanking time
T_{d}	Switch turn-on duration
T_{corr}	The correction time of V_{mag} calculation
T_{fo}	The period of v_{fo}

T_t	Voltage averaging period
t	Time variable
V_{CC}	Positive op-amp supply voltage
V_{EE}	Negative op-amp supply voltage
V_{amp}	The amplitude of v_a, v_b and v_c
V_{corr}	The correction voltage of V_{mag} calculation
V_{dd}	Diode voltage drop
V_{dt}	IGBT voltage drop
V_{eq}	The amplitude of v_{eq}
V_{mag}	The amplitude of v_{sqr}
$V_{mag(M)}$	The amplitude of v_{sqr} at maximum output power
V_{nim}	NIM voltage amplitudes
$V_{nim(M)}$	NIM amplitude at maximum output power
V_o	The amplitude of v_o
V_{off}	The offset voltage of a DHC circuit
V_p	The amplitude of v_p
V_s	The amplitude of v_s
$V_{sim(M)}$	SIM amplitude at maximum output power
v	Voltage
v_a	The Phase A voltage of a three-phase input
v_b	The Phase B voltage of a three-phase input
v_c	The Phase C voltage of a three-phase input
v_{co}	DHC output voltage
v_{cp}	Voltage over C_p
v_{dis}	Distorted sinusoidal voltage
v_{eq}	The equivalent voltage of a modulation
v_{fo}	The filter output voltage of a ZCD circuit
v_h	The hysteresis voltage of a DHC circuit

v_{nim}	The equivalent voltage of NIM
v_{o}	Output voltage
v_{p}	The injection voltage of MMCFS
$\hat{v}_{\mathrm{p}}$	The peak voltage of v_{p}
v_{s}	The secondary-side voltage of MMCFS-IPT
$\hat{v}_{\mathrm{s}}$	The peak voltage of v_{s}
v_{sqr}	Square-wave voltage
v_{z}	The output voltage of an edge-triggering circuit
$\mathbb{Z}$	Integer number
Z_{t1}, Z_{t2}	The impedances of a series-none IPT system

Greek letter symbols:

β_1	The ratio of L_{p} and L_{s}
β_2	The ratio of L_{p} and C_{p}
γ	Load matching factor
ζ	Damping ratio
η_{link}	Link efficiency
Θ	Resonant frequency variable
ω	Frequency in radian
ω_{l}	Line voltage frequency in radian
ω_0	Resonant frequency in radian
π	The ratio of a circle's circumference to its diameter
Ψ	Resonant frequency variable

1. Introduction

This chapter briefly summarizes past work on inductive power transfer and the characteristics of AC/AC converters forming the basis of this dissertation. It begins with an explanation of the background and motivation, leading to the research questions, followed by the objectives and the scientific contributions arising from this research. Finally, the structure of this dissertation is outlined in the last part of this chapter.

1.1 Background and Motivation

The safety, reliability, and mobility of the power delivery circuit, such as a battery charger, can be improved by adding an Inductive Power Transfer (IPT) feature to the circuit. For example, system safety in the power delivery circuit can be increased by eliminating the need for a power cable and connectors, thus lowering the risk of sparking and electric shock. IPT also increases reliability, since the power delivery process involves no moving parts on the transmitter and receiver circuits, as well as provides good mobility for the recipient during power transfer. IPT uses a magnetic induction principle to supply power between two circuits separated by a certain distance. Both transmitter and receiver circuits are magnetically connected through a coupled coil to send electric power [1–6].

A typical IPT system that is connected to a three-phase alternating current (AC) power source consists of multiple power conversion stages on the primary side to create a magnetic link. The stages are typically formed by combining a rectifier and an inverter through an energy storage element (e.g., a capacitor or an inductor), forming a Rectifier-Inverter (RI) topology. In this topology, semiconductor switches are commonly arranged in the full-bridge connection on both rectifier and inverter sides, in which the neutral line is disconnected. In practice, the current commutation of RI is handled by at least two switches on each side and the energy storage, where losses occur in each element. One approach to reduce these losses and the structural complexity is to replace the RI topology

with a single-stage direct converter, also known as a matrix converter. The converter can directly connect the power source and an electric load without using the energy storage element [1, 2, 7–10]. One such converter is the three-phase to single-phase Midpoint Matrix Converter using a Free-wheeling Switch (MMCFS), which only employs four bi-directional switches [7, 8]. MMCFS only uses two semiconductor switches for the current commutation during its operation. As a result, the topology of MMCFS possesses lower structural complexity and conduction losses than those of the RI. Although this matrix topology generally offers better overall power transfer efficiency than RI, it relies on the phase-shift modulation that utilizes a hard-switching strategy to control power transfer. This type of modulation can introduce a significant switching loss during the turn-on and turn-off transitions at a partial load, especially when employing silicon-based semiconductor devices. [8, 11].

1.2 Research question and objective

To improve the MMCFS conversion efficiency at the partial load, a soft-switching-based modulation is needed. A modulation scheme based on current injection and Free-Wheeling Oscillation (FWO) was presented in [2] and [12], for a single-phase to single-phase direct AC/AC converter. This scheme is soft switching in which the Zero-Current Switching (ZCS) transition is used to reduce the switching power loss. In this scheme, the direct converter varies the density of current injection with respect to FWO to control power transfer. Thus, this modulation can be considered as a variation of Pulse-Density Modulation (PDM) [11, 13]. Additionally, the complexity of the series-series IPT system with high quality and coupling factors can be reduced by using the series-none configuration, since this would remove the secondary side compensation capacitor [6, 10, 14]. If the soft-switching approach and the series-none configuration can be utilized in MMCFS, they could potentially enhance conversion efficiency under all load conditions and reduce one passive element. To determine the feasibility of these improvements, this dissertation seeks to find answers to the following three research questions:

- How could the PDM be used in the MMCFS?
- How could the MMCFS be implemented with PDM in an actual IPT system?
- What are the system characteristics (e.g., voltage, current and efficiency) of the PDM-based series-none IPT system?

To answer these research questions, the dissertation aims to achieve three objectives:

1. Develop a computer simulation for the MMCFS-based IPT (MMCFS-IPT) system that is driven by the PDM.
2. Quantify the MMCFS-IPT behavior through mathematical models.
3. Build an actual MMCFS-IPT prototype to validate the simulation and the models.

To narrow the research topic, since the MMCFS is assumed to be connected to a three-phase utility supply through an input filter, input harmonics analysis will remain outside the scope of this dissertation. Because the coupling factor between primary and secondary coils is also fixed, dynamic IPT operation will not be discussed in this work.

1.3 Scientific contribution

This dissertation groups its scientific contributions into three main categories: modulation strategy, system behavior description, and practical implementation.

In Publications V and VI, two PDM-based modulation strategies were proposed and described for the MMCFS-IPT: Non-successive Injection Modulation (NIM) and Successive Injection Modulation (SIM). NIM only performs current injections from one of the input three-phase sources. SIM uses two input phases to perform the injections. In both modulations, output power is controlled by varying the number of injections with respect to FWOs. This variation is achieved using an on-off current control. To analyze the behavior of the PDM-based MMCFS-IPT, an equivalent output voltage was derived for both modulations.

Publications I and VI describe the series-none and series-series MMCFS-IPT behavior. For a unidirectional power transfer case, these studies show that there is a direct relationship between current damping ratio, link efficiency, voltage gain and the MMCFS-IPT coupling factor. Maximum link efficiency can be achieved by tuning the MMCFS-IPT load with coupling factor information. In addition to unidirectional power, the MMCFS-IPT is also capable of transferring bi-directional power using the series-series configuration. The ability is demonstrated at the simulation level in Publication IV.

In practice, a kick-start process is beneficial for the series-none MMCFS-IPT, which is described in Publications III and VI. The kick-start process is based on the direct current (DC) resonant charging principle by taking advantage of the MMCFS-IPT topology. Another practical requirement is a Zero-Crossing-Detector (ZCD) circuit, which is explained in Publication II. The ZCD circuit is utilized to approximate current zero-crossing for executing the injection and FWO. Furthermore, to drive the converter switches,

Publication VI proposes a multistep switching method for preventing short and open circuits during the MMCFS-IPT operation.

1.4 Dissertation outline

The rest of this dissertation is organized as follows. Chapter 2 introduces common methods for three-phase to single-phase AC-AC conversion, including indirect and direct approaches. The indirect method is represented by a Voltage Back-to-Back (VB2B) topology, whereas the direct case presents midpoint and bridge matrix configurations. The chapter also discusses the MMCFS and its ZCS-based modulation in detail. Chapter 3 describes IPT application of the MMCFS in terms of a self-oscillating series-none IPT system and its electrical characteristics. The characteristics are obtained through derivations of dynamic and steady-state mathematical equations of the system. The chapter closes by briefly presenting the bi-directional power transfer concept for a series-series MMCFS-IPT. Chapter 4 elaborates a prototype for unidirectional power MMCFS-IPT, as well as provides practical requirements for implementing the actual circuit, such as methods to start the converter and to switch its semiconductor devices. Experimental data are analyzed and compared with theoretical calculations and simulation results. Finally, Chapter 5 concludes this dissertation by recommending areas for future work.

2. Three-Phase to Single-Phase AC-AC Conversion

This chapter introduces selected topologies for AC-AC conversion, with an emphasis on MMCFS. Both indirect and direct approaches are briefly explained in Section 2.1. Section 2.2 describes the fundamental operation of MMCFS and its ZCS-based modulation strategies.

2.1 Indirect and Direct AC-AC Conversion Methods

Electric equipment operates using electric power with certain voltage and current requirements. To power AC equipment from a three-phase AC utility grid that has different electrical characteristics, an AC-AC converter circuit is needed for conversion. The conversion method is based on either an indirect or a direct approach [15–17].

2.1.1 Indirect method using an intermediate capacitor

Three-phase to single-phase AC-AC conversion can be achieved using a pulse-width modulation (PWM) rectifier and a PWM inverter, connected through an intermediate capacitor. The arrangement forms a VB2B topology, as can be seen from the schematic in Figure 2.1. This VB2B topology consists of five converter legs in total, in which each leg consists of two insulated-gate bipolar transistors (IGBT) and its own anti-parallel diode. Alternatively, the IGBT can be replaced by other types of transistors, such as a field-effect transistor. For the sole purpose of unidirectional power transfer operation, all IGBTs and inductances on the rectifier side can be omitted, thus transforming the VB2B to RI [8, 16, 18].

The rectifier side is comprised of three input inductors, each of which is connected to one converter leg. Since each inductor-leg connection resembles a boost converter, the rectifier has a voltage step-up capability on the capacitor C_{DC}. Consequently, the capacitor voltage can be greater than the peak of the three-phase input [18,19]. Some modulation strategies have been presented for operating the rectifier [17,18,20]. These strategies

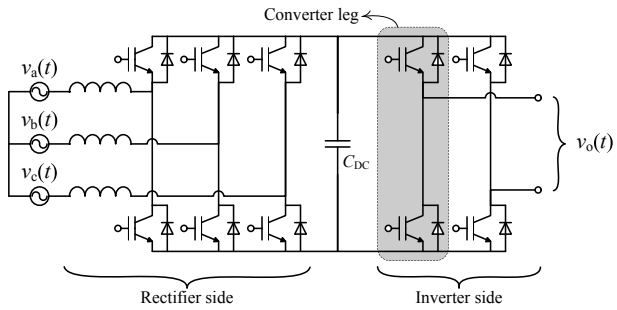

Figure 2.1. Topology of VB2B converter, in which the intermediate capacitor C_{DC} decouples the input and output stages.

utilize the switches on the three legs to produce a desired voltage on the C_{DC}.

The PWM inverter consists of two legs and can convert the DC taken from C_{DC} to a time-averaged single-phase AC. The output AC voltage $v_o(t)$ can have amplitude and frequency which differ from that of the three-phase input [15–18]. The square-wave and PWM-based modulations necessary for driving the inverter have been explained in [17].

The VB2B topology is an indirect approach, since the conversion involves two circuit stages (rectification and inversion). Therefore, the inverter input is independent from that of the rectifier, since both stages are decoupled to a large extent. However, in practice, C_{DC} can have a relatively large physical volume. Moreover, if an electrolytic capacitor is used, a poor lifetime can be expected [18].

2.1.2 Direct method using a matrix converter

To increase system reliability, the number of semiconductor switches in a converter circuit needs to be low. A reduced component quantity also leads to increased power density in the system. In the case of AC-AC conversion, this goal can be achieved using a matrix converter. The converter is a single-stage force-commutated type for simultaneous amplitude and frequency transformation. Its switching network comprises an array of controlled bi-directional switches, which can conduct and block current in forward and reverse directions. Furthermore, the matrix converter does not have an intermediate energy storage element as in the VB2B case [18, 19, 21]. Two variants of the three-phase to single-phase matrix converter are shown in Figure 2.2 in which all switches are bi-directional. The midpoint configuration has a lower number of switches than the bridge, however the configuration involves a neutral line connection [22, 23].

With the matrix topology, each input ($v_a(t)$, $v_b(t)$ or $v_c(t)$) can be directly connected to the output $v_o(t)$. If it is assumed that the output is connected to an inductive load, two switching states must be avoided during its op-

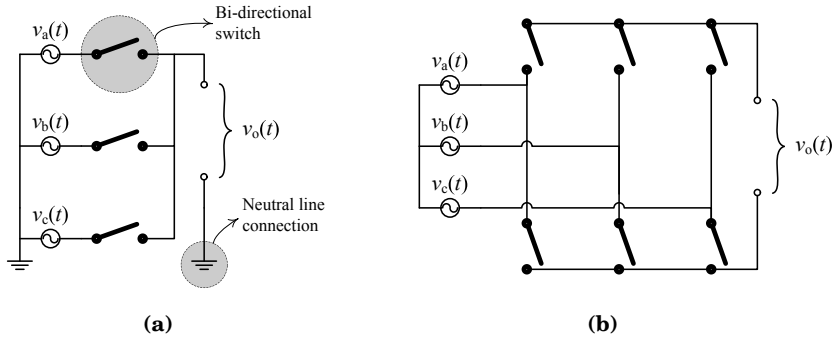

Figure 2.2. Two types of three-phase to single-phase matrix converter topology. (a) Midpoint configuration. (b) Bridge configuration.

eration, as illustrated in Figure 2.3. These prohibitions can be applied to either midpoint or bridge configuration. The first prohibition is connecting two input switches at the same time, since this would cause a short circuit. The second prohibition is opening all switches connected to the load simultaneously when the inductor is energized. To avoid these prohibitions, a matrix converter requires a multistep commutation strategy [21, 24].

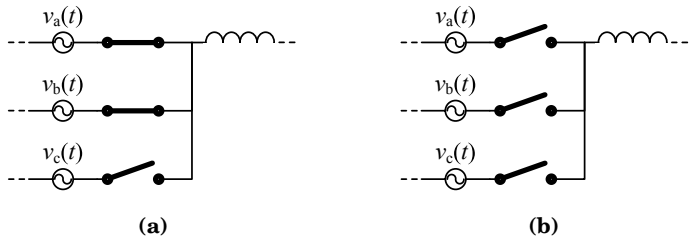

Figure 2.3. Two switching prohibitions of matrix converter. (a) Two input switches are connected together (short-circuit). (b) Energized inductor is isolated (open-circuit).

By utilizing high switching frequency in one of the modulation schemes described in [21] and [24], a matrix converter can generate a time-averaged output voltage with variable amplitude and frequency. In terms of the output, the matrix topology does not have an inherent boost capability like that of the VB2B converter [18, 19, 21].

Bi-directional switch

The main switching element of a matrix converter is the bi-directional switch, which can be built by combining discrete semiconductor devices, such as IGBTs and diodes. Four types of bi-directional switch that can be constructed from such devices are illustrated in Figure 2.4 [21, 25].

For the bridge structure, only one gate driver is needed since it only contains one transistor. However, it suffers from a larger degree of power loss than the other configurations, as the current must travel through three components (i.e., one transistor and two diodes) during conduction.

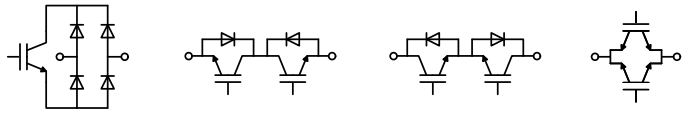

Figure 2.4. Four types of bi-directional switch. (a) Bridge structure. (b) Common-collector structure. (c) Common-emitter structure. (d) Parallel structure.

The common-collector and common-emitter structures are constructed from two pairs of transistor with its own anti-parallel diode. In this case, one transistor and one diode are involved in current conduction. Finally, a reverse-blocking IGBT can be used to form a bi-directional switch by connecting two of the IGBT in parallel. This arrangement enables conduction loss to be minimized in only one IGBT. In terms of common-collector, common-emitter and parallel structures, the transistors are controlled using two gate drivers powered by their isolated power supplies. [21, 25].

In the case of three-phase to single-phase AC-AC conversion, a midpoint or bridge matrix converter employing bi-directional switches using the parallel structure has a lower number of power switches than those of the VB2B topology.

2.2 MMCFS Topology

MMCFS topology and its basic working principle are mainly described in Publications V and VI. Figure 2.5 provides a schematic of the MMCFS consisting of four bi-directional switches (with the common-emitter arrangement) and a network of resistor R, capacitor C, and inductor L (RCL) as a load. The RCL load is chosen to represent IPT application. The three-phase input is connected to the inductive load L through the input-side switches (i.e., $\{s_{ap},s_{an}\}$, $\{s_{bp},s_{bn}\}$ and $\{s_{cp},s_{cn}\}$). In addition, one bi-directional switch comprises s_{dn} and s_{dp} is attached in parallel with the RCL to create a free-wheeling path. This MMCFS topology was previously proposed by two different authors in [8] and [22] and can also be seen as an expansion of the direct converter described in [2]. Since the RCL load is driven at its resonant frequency, the converter load becomes purely resistive [2, 26]. Because of this mode of operation, the resonant tank can be seen as a part of the topology.

2.2.1 Current commutation

There are two types of current commutation in the MMCFS with RCL load, as illustrated in Figure 2.6. In each illustration, a bold line with an

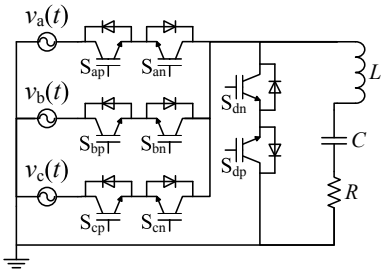

Figure 2.5. Topology of MMCFS constructed by IGBTs and anti-parallel diodes.

arrow marks the flow of primary circuit current $i_p(t)$. The clockwise flow is defined as a positive direction, whereas the counter-clockwise is a negative one. From Figures 2.6(a) and 2.6(b), it can be seen that injection lets $i_p(t)$ flow between the voltage source (in this case Phase A) and the RCL network. This commutation concept can also be applied using Phase B and Phase C, through their respective input switches. In the case of FWO, since the RCL is isolated from the source, the $i_p(t)$ oscillates only in the free-wheeling path, as shown in Figures 2.6(c) and 2.6(d). Both types of commutation are used in a modulation strategy to deliver power from the three-phase input to the RCL load.

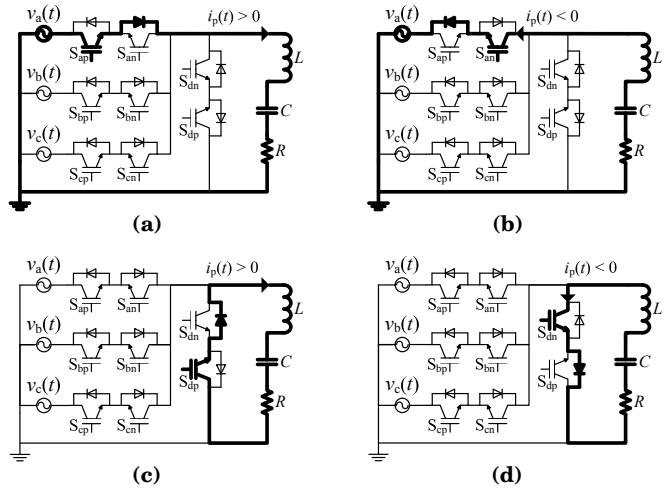

Figure 2.6. Four possible current commutations of MMCFS when Phase A is used as an injection source. (a) Positive injection. (b) Negative injection. (c) Positive FWO. (d) Negative FWO.

2.2.2 Modulation strategy

Two types of ZCS-based modulation strategy were developed for the MMCFS in this research work: NIM and SIM. NIM is explained in Publication VI, whereas SIM is described in Publication V.

NIM strategy

NIM executes injection and FWO at a maximum absolute value region of the three-phase input, which can be expressed as

$$\mathrm{Max}(v) = \mathrm{Max}(|v_a(t)|, |v_b(t)|, |v_c(t)|). \tag{2.1}$$

Figure 2.7 shows NIM operation for a maximum output power mode in which the switching period is exaggerated for clarity. As can be seen in the figure, a three-phase voltage source with an amplitude of V_{amp} has been divided into two Max(v) regions (i.e., Max(v) = $v_a(t)$ and Max(v) = $v_c(t)$). The injection voltage is marked by bars with diagonal stripes, while FWO is represented by spaces between the bars along the t axis. The $v_p(t)$, which is a combination of the two commutations appears over the series RCL load. In the figure, at Max(v) = $v_c(t)$, three switching signals are involved in NIM operation: $s_{cn}(t)$, $s_{dp}(t)$ and $s_{dn}(t)$. These signals correspond to the switch S_{cn}, S_{dp} and S_{dn}, respectively (see Figure 2.6). In this case, the S_{cn} performs negative current injection, whereas FWO is executed by S_{dp} and S_{dn}. The on-off transition of each signal happens at the zero-crossing of $i_p(t)$ to reduce switching loss. To manage power transfer between the input and the RCL, the density of injections is varied with respect to FWOs. Lesser injections lead to a lower power transfer, as shown in Figure 2.8. Due to the variable density, this form of modulation can be classified as PDM [11].

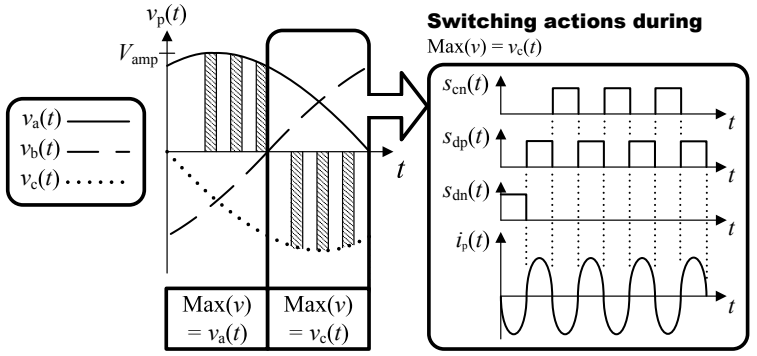

Figure 2.7. NIM illustration of MMCFS at maximum output power mode. Switching actions during Max(v) = $v_c(t)$ are highlighted.

For a steady-state analysis, $v_p(t)$ needs to be approximated by a sinusoidal voltage $v_{nim}(t)$, which can be accomplished by using the power equality approach developed in Publication VI. Figure 2.9 illustrates the approximation for the NIM case involving a square voltage $v_{sqr}(t)$. The initial step is to calculate $v_{sqr}(t)$ that can produce an equal output power as the $v_p(t)$. The final step is a fundamental extraction of $v_{nim}(t)$ from $v_{sqr}(t)$. The switching frequency of NIM is equal to the $i_p(t)$ frequency, and the period is marked by T_0. Additionally, variable T_t indicates two Max(v) regions,

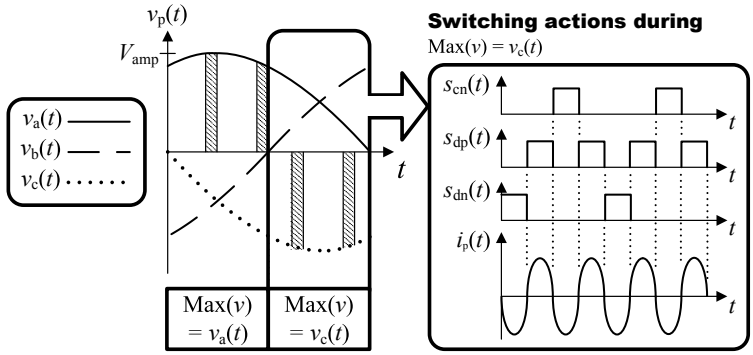

Figure 2.8. NIM operation of MMCFS at partial load. Switching actions during $\mathrm{Max}(v) = v_c(t)$ are highlighted.

which is $2\pi/3$ rad, or 6.667 ms for a 50 Hz input line frequency. The two Max(v) regions are chosen because $v_p(t) = v_p(t + T_t)$.

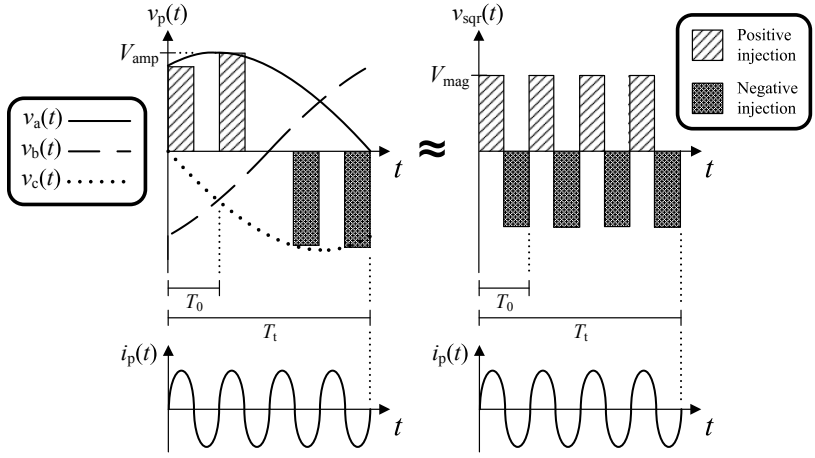

Figure 2.9. Square voltage approximation of $v_p(t)$ for NIM during Max(v) equals $v_a(t)$ and $v_c(t)$. In this illustration, T_0 is exaggerated to $T_t/4$ for clarity.

The approximation calculation needs the following assumptions: active power is contributed by only one frequency component of $v_p(t)$ and $i_p(t)$, $T_0 << T_t$ and $T_t = nT_0$, where $n \in \mathbb{Z}$. Under these assumptions, the dashed area of $v_p(t)$ and $v_{sqr}(t)$ are equal. If the average power for $v_p(t)$ and $v_{sqr}(t)$ are indicated by P_p and P_{sqr}, respectively, the equivalent voltage derivations are given as

$$P_p = \frac{1}{T_t}\int_0^{T_t} v_p(t) i_p(t)\mathrm{d}t \approx P_{sqr} = \frac{1}{T_t}\int_0^{T_t} v_{sqr}(t) i_p(t)\mathrm{d}t, \tag{2.2}$$

$$v_p(t)\mathrm{d}t \approx v_{sqr}(t)\mathrm{d}t, \tag{2.3}$$

$$v_p(t)\mathrm{d}t \approx V_{mag} \sum_{k_0=0}^{k_0=(N_0-1)} \frac{T_0}{2}, \qquad k_0 = \mathbb{Z}, \quad N_0 \approx \frac{T_t - 0}{T_0/2}, \quad T_t = \frac{2\pi}{3\omega_l}, \tag{2.4}$$

$$V_{\text{amp}}\left[\sum_{k_1=0}^{k_1=(N_1-1)}\sin\left(\omega_{\text{l}}k_1\frac{T_0}{2}+\frac{\pi}{3}\right)+\sum_{k_1=N_1}^{k_1=(N_2-1)}\sin\left(\omega_{\text{l}}k_1\frac{T_0}{2}+\frac{4\pi}{3}\right)\right]\frac{T_0}{2}\approx V_{\text{mag}}T_{\text{t}}, \tag{2.5}$$

$$k_1=2\mathbb{Z},\quad N_1\approx\frac{T_{\text{t}}/2-0}{T_0/2},\quad N_2\approx\frac{T_{\text{t}}-T_{\text{t}}/2}{T_0/2}, \tag{2.6}$$

where V_{mag} is the amplitude of $v_{sqr}(t)$ and ω_{l} is the input line frequency in radian. Because of the n assumption, N_0, N_1 and N_2 are rounded. On the left side of (2.5), two summations correspond to the region of $\text{Max}(v)=v_{\text{a}}(t)$ and $\text{Max}(v)=v_{\text{c}}(t)$, respectively. Since both regions can be assumed to have equal pattern and size, both summations can be combined. The amplitude V_{mag} can then be expressed as

$$V_{\text{mag}}\approx 2V_{\text{amp}}\left[\sum_{k_1=0}^{k_1=(N_1-1)}\sin\left(\omega_{\text{l}}k_1\frac{T_0}{2}+\frac{\pi}{3}\right)\right]\frac{T_0}{2T_{\text{t}}}. \tag{2.7}$$

The amplitude of $v_{\text{nim}}(t)$ is obtained by extracting the fundamental harmonic of $v_{sqr}(t)$ as follows:

$$V_{\text{nim}}=V_{\text{mag}}\frac{4}{\pi}\frac{1}{\sqrt{2}}. \tag{2.8}$$

The $\sqrt{2}$ division produces root mean square (RMS) value.

At maximum output power operation, the $v_{\text{sqr}}(t)$ amplitude can be approximated by performing an integration over the two $\text{Max}(v)$ regions, and dividing the result by two. Using this approach, the amplitude can be expressed as

$$V_{\text{mag(M)}}\approx\frac{3V_{\text{amp}}}{2\pi}. \tag{2.9}$$

The "(M)" subscript indicates the maximum output configuration.

SIM strategy

SIM is explained in Publication V, and uses two input phases having an opposite sign to perform injection. The phases can be obtained from a minimum absolute value calculation as follows:

$$\text{Min}(v)=\text{Min}(|v_{\text{a}}(t)|,|v_{\text{b}}(t)|,|v_{\text{c}}(t)|). \tag{2.10}$$

At this region, when one phase is equal to $\text{Min}(v)$, the other two will have a maximum peak-to-peak range. Figure 2.10 illustrates SIM operation for maximum output power mode, in which the three-phase input with an amplitude of V_{amp} is divided into two $\text{Min}(v)$ regions. Injection voltages are indicated by bars with diagonal stripes, where one injection is followed by another one with a different polarity. It can be seen from the figure that there is no FWO in this maximum output mode, hence S_{dn} and S_{dp}

are not operated. At Min(v) = $v_a(t)$, injections are performed from Phase B and Phase C through S_{bp} and S_{cn}, respectively. In common with NIM, current zero-crossing transition is also used to operate converter switches. SIM operation at partial load is shown in Figure 2.11. In this case, the injections are sparser than the case provided in Figure 2.10, and the FWO is utilized.

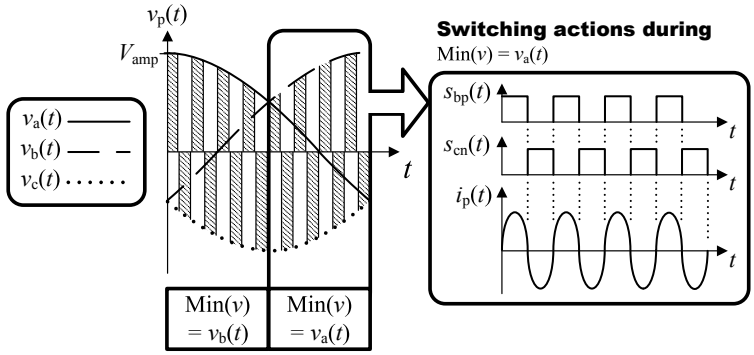

Figure 2.10. SIM illustration of MMCFS at maximum output power. Switching actions during Min(v) = $v_a(t)$ are highlighted.

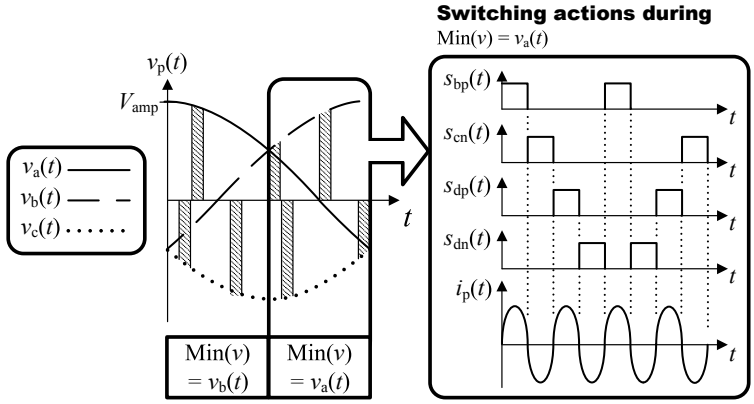

Figure 2.11. SIM operation at partial load. Switching actions during Min(v) = $v_a(t)$ are highlighted.

The equivalent input voltage of SIM is also needed for steady-state analysis. Its calculation uses the same approach as in the V_{nim} case. The approximation process is illustrated in Figure 2.12. Analogous to NIM, variable $v_{sqr}(t)$ with an amplitude of V_{mag} represents a square voltage equivalent of the $v_p(t)$. The switching period is denoted by T_0, which is equivalent to the primary resonant current period. In this case, T_t indicates the two Min(v) regions, which equals to two Max(v) regions. To calculate the equivalent voltage at maximum output operation, an integral approach is used. The approximation assumptions and steps are the same as those used to calculate NIM, which begins with (2.2). For SIM, V_{mag} can be expressed as

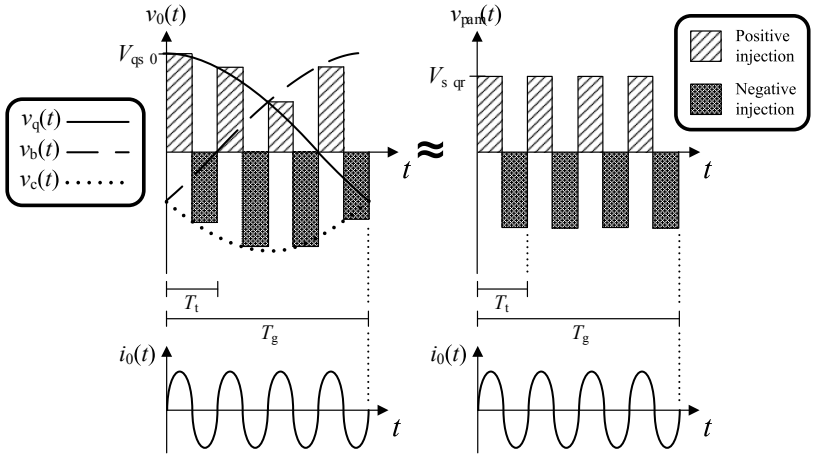

Figure 2.12. Square voltage approximation of $v_p(t)$ for SIM during Min(v) equals $v_b(t)$ and $v_a(t)$. The value of T_0 is exaggerated to $T_t/4$ for clarity.

$$V_{mag(M)}T_t \approx \frac{1}{2}\left[\int_0^{T_t/2} V_{amp}\sin\left(\omega_1 t+\frac{\pi}{2}\right)dt+\left|\int_0^{T_t/2} V_{amp}\sin\left(\omega_1 t+\frac{7\pi}{6}\right)dt\right|\right.$$
$$\left.+\int_{T_t/2}^{T_t} V_{amp}\sin\left(\omega_1 t-\frac{\pi}{6}\right)dt+\left|\int_{T_t/2}^{T_t} V_{amp}\sin\left(\omega_1 t+\frac{7\pi}{6}\right)dt\right|\right], \quad (2.11)$$

therefore, the amplitude of $v_{sqr}(t)$ can be written as

$$V_{mag(M)} \approx \frac{3\sqrt{3}V_{amp}}{2\pi}. \quad (2.12)$$

Finally, the equivalent voltage at a maximum output is obtained by extracting the fundamental of $v_{sqr}(t)$ as follows:

$$V_{sim(M)} = V_{mag(M)}\frac{4}{\pi}\frac{1}{\sqrt{2}} = \frac{6\sqrt{3}V_{amp}}{\sqrt{2}\pi^2}. \quad (2.13)$$

The value is in the RMS form due to the $\sqrt{2}$ division.

For the maximum output power operation, the ratios of approximated voltage and average power between NIM and SIM can be calculated as

$$\frac{V_{sim(M)}}{V_{nim(M)}} = \left(\frac{6\sqrt{3}V_{amp}}{\sqrt{2}\pi^2}\right)\Big/\left(\frac{6V_{amp}}{\sqrt{2}\pi^2}\right) = \sqrt{3} \approx 1.732, \quad (2.14)$$

$$\frac{P_{sim(M)}}{P_{nim(M)}} = \frac{V_{sim(M)}^2}{V_{nim(M)}^2} = 3. \quad (2.15)$$

Variable $V_{nim(M)}$ was obtained by combining equation (2.8) and (2.9). Equation (2.15) implies that the SIM produces three times more power than NIM in this case.

Since both modulation methods are a variation of PDM, the power transfer increment or decrement is discrete. A smoother transition can be achieved by increasing the resonant frequency of the IPT system.

2.2.3 Galvanic isolation

A coupled inductor/coil can be applied on the RCL load to provide a galvanic isolation and mobility between the MMCFS and the R. The usage transforms the schematic in Figure 2.5 to that shown in Figure 2.13, in which the RCL load of the converter is divided into two parts. The first part is the inductor-capacitor (LC) circuit on the primary side, which is denoted by the "p" subscript, and the second part is the inductance on the secondary side indicated by the "s" subscript, which is attached to R. Both sides are magnetically connected through a mutual inductance, which can be expressed as

$$M = k\sqrt{L_{\mathrm{p}}L_{\mathrm{s}}}, \tag{2.16}$$

where k is a coupling factor between the coupled coil, which depends on its physical properties [1, 26]. Henceforth, the network of capacitor C_{p} and the coupled inductor (i.e., L_{p} and L_{s}) will be referred to as a LC-L network in the following chapters.

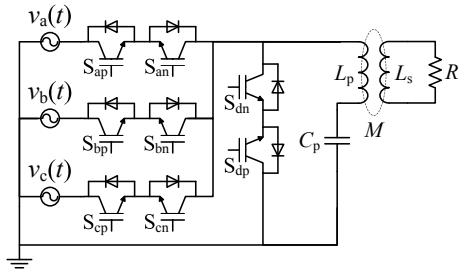

Figure 2.13. Applying galvanic isolation to MMCFS topology.

3. Inductive Power Transfer Application of MMCFS

This chapter discusses the application of MMCFS in a stationary IPT system. Section 3.1 briefly introduces a typical series-series IPT configuration connected to a three-phase power source. The series-none MMCFS-IPT application is presented in Section 3.2, and the IPT theoretical models are derived in Section 3.3. These models describe the characteristics of the series-none IPT system, such as resonant frequency, output power, link efficiency, voltage gain, and damping behavior. Finally, this chapter closes with an explanation of the MMCFS application in a series-series IPT system capable of bi-directionally transferring power.

3.1 Series-series IPT circuit configuration

The circuit diagram of a typical series-series IPT system connected to a three-phase AC source can be seen in Figure 3.1, in which the primary side comprises an AC/AC converter that can be either the indirect or direct type. This AC/AC converter is connected to a series LC network (i.e., L_p and C_p) on the primary side. The LC network on the secondary side (i.e., L_s and C_s) is attached to a pick-up circuit consisting of a rectifier and a DC/DC converter. The rectifier converts AC to DC for powering the load (e.g., electric equipment and a battery), while the DC/DC converter controls the current or voltage delivered to such a load. Both circuit sides are physically separated and magnetically coupled through L_p and L_s coils. Such physical separation usually exhibit a low k characteristic. Since the primary and secondary LC networks are identical, namely $L_\mathrm{p} = L_\mathrm{s}$ and $C_\mathrm{p} = C_\mathrm{s}$, the networks have equal resonant frequency (ω_0) [1, 3, 5, 27, 28].

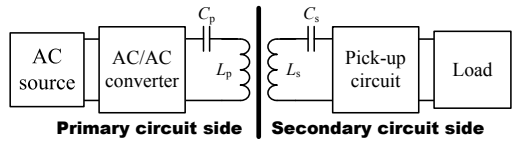

Figure 3.1. Series-series IPT system.

The inverter side of the AC/AC converter is operated at ω_0 of the LC networks to cancel leakage inductance of both L_p and L_s. This cancellation minimizes a volt-ampere rating of the converter and improves power transfer efficiency between the source and the load [1, 27, 28].

3.2 MMCFS-based self-oscillating IPT system

Descriptions of series-none MMCFS-IPT are provided in Publications V and VI. In this case, the MMCFS is utilized as an AC/AC converter as can be seen from the circuit diagram in Figure 3.2. Compared to the series-series IPT configuration, this series-none removes the capacitor C_s on the secondary side [1, 8, 10].

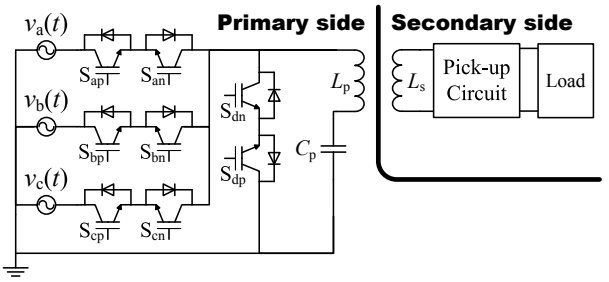

Figure 3.2. Series-none IPT system using MMCFS on its primary side.

3.2.1 Current control

As discussed in Section 2.2.2, the number of injections is varied to control the power transfer between the primary and secondary sides of the IPT system. This variation can be produced by an on-off current controller implemented on the primary circuit side. The flowchart of such a controller is shown in Figure 3.3. The diagram indicates that when the IPT system is turned on for the first time (i.e., $I_\mathrm{p} < I_\mathrm{lim}$), it must perform an initial stage to reach a steady-state condition. This stage uses a kick-start block to trigger $i_\mathrm{p}(t)$ oscillation in the LC network on the primary side. The control algorithm is executed after the IPT system passes the initial stage, namely $I_\mathrm{p} < I_\mathrm{lim}$ is FALSE. When the ON state is TRUE, the number of FWOs will be adjusted (i.e., increased or decreased) to maintain the I_p close to the I_ref. As a result, the power transfer between the primary and secondary sides can be controlled. The MMCFS-IPT is turned off by setting the ON state to FALSE, during which the converter utilizes only FWO to completely remove the oscillating current in the primary-side LC network.

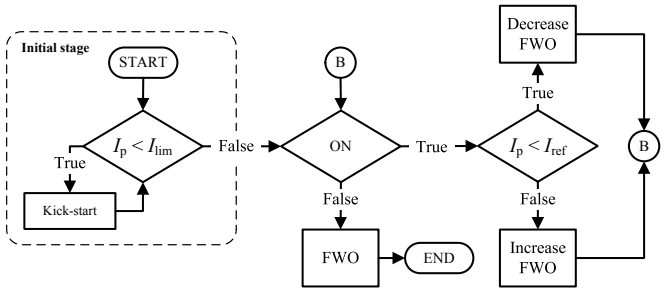

Figure 3.3. The flowchart of on-off current control used in the MMCFS-IPT system.

3.3 Theoretical model of a MMCFS-based series-none IPT system

Simplified circuit models and mathematical equations were developed to analyze the electrical characteristics of a series-none MMCFS-IPT system. These models and equations are based on Publications I and VI. In terms of the models, they are simplified versions of the circuit in Figure 3.2, as can be seen in Figure 3.4. In the figure, $v_{eq}(t)$ replaces the three-phase input and switching network of the MMCFS-IPT. The amplitude of $v_{eq}(t)$ is determined by the converter modulation method, which can be either V_{nim} or V_{sim} (see Section 2.2.2). The components in the gray area (i.e., a rectifier, a smoothing capacitor C_L and a resistor R_L) represents the pick-up circuit and the load in Figure 3.2. Parasitic resistances of the primary and secondary coils are shown and denoted by R_p and R_s, respectively. Additionally, currents that flow in the circuits are denoted by $i_p(t)$ and $i_s(t)$.

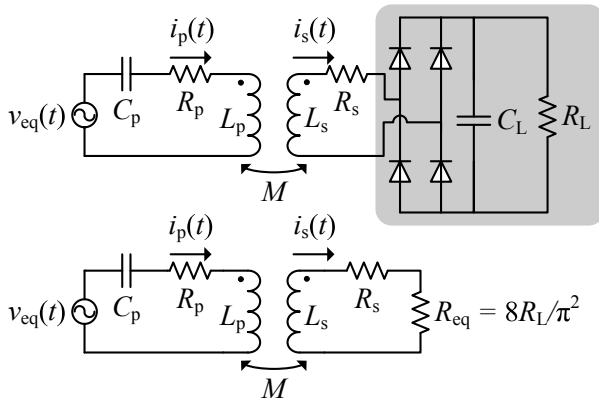

Figure 3.4. Two simplified circuit models of a MMCFS-IPT system.

In Figure 3.4, the top schematic can be simplified by representing components in the gray area with an AC equivalent load R_{eq} [29]. Thus, this approach produces the bottom schematic that has the following steady-

state equations:

$$\begin{cases} V_{\text{eq}} = \frac{\mathbf{i_p}}{\text{j}\omega C_\text{p}} + \mathbf{i_p}\text{j}\omega L_\text{p} + \mathbf{i_p}R_\text{p} - \mathbf{i_s}\text{j}\omega M, \\ 0 = \mathbf{i_s}R_\text{eq} + \mathbf{i_s}\text{j}\omega L_\text{s} + \mathbf{i_s}R_\text{s} - \mathbf{i_p}\text{j}\omega M, \end{cases} \qquad V_{\text{eq}} = \begin{cases} V_{\text{nim}} & \text{if NIM} \\ V_{\text{sim}} & \text{if SIM.} \end{cases} \tag{3.1}$$

The expression of M was given in (2.16), and ω is the frequency of $v_{\text{eq}}(t)$ in rad/s. The electrical characteristics of the MMCFS-IPT are derived based on an assumption that all circuit components are ideal.

In order to determine a relationship between voltage and current, the equations provided in (3.1) are combined to form

$$V_{\text{eq}} = \mathbf{i_p}Z_{\text{t1}} = \mathbf{i_s}Z_{\text{t2}}, \tag{3.2}$$

$$Z_{\text{t1}} = \frac{\omega^2 M^2 (R_\text{s} + R_\text{eq})}{\omega^2 L_\text{s}^2 + (R_\text{s} + R_\text{eq})^2} + R_\text{p} + \text{j}\left[\omega L_\text{p} - \frac{1}{\omega C_\text{p}} - \frac{\omega^3 M^2 L_\text{s}}{\omega^2 L_\text{s}^2 + (R_\text{s} + R_\text{eq})^2}\right], \tag{3.3}$$

$$Z_{\text{t2}} = \left(\frac{R_\text{s} + R_\text{eq} + \text{j}\omega L_\text{s}}{\text{j}\omega M}\right)\left(R_\text{p} + \frac{1}{\text{j}\omega C_\text{p}} + \text{j}\omega L_\text{p}\right) - \text{j}\omega M. \tag{3.4}$$

These equations are obtained by either eliminating $\mathbf{i_p}$ or $\mathbf{i_s}$ term through substitution.

3.3.1 Resonant frequency

The ω_0 of the MMCFS-IPT load is used to switch the converter of the IPT system for resonant operation. At this mode of operation, the imaginary part of (3.3) is equal to zero, and the equation can be arranged into a quartic form as

$$\omega_0 L_\text{p} - \frac{1}{\omega_0 C_\text{p}} = \frac{\omega_0^3 M^2 L_\text{s}}{\omega_0^2 L_\text{s}^2 + (R_\text{s} + R_\text{eq})^2}, \tag{3.5}$$

$$C_\text{p}(L_\text{p} L_\text{s}^2 - M^2 L_\text{s})\omega_0^4 + [L_\text{p} C_\text{p}(R_\text{s} + R_\text{eq})^2 - L_\text{s}^2]\omega_0^2 - (R_\text{s} + R_\text{eq})^2 = 0. \tag{3.6}$$

Since this quartic equation has a bi-quadratic form, the roots of the equation can be obtained through the quadratic formula. These roots can be expressed as

$$\omega_0 = \pm\sqrt{-\Theta \pm \Psi}, \tag{3.7}$$

$$\Theta = \frac{1}{2L_\text{p}^2}\left[\frac{{\beta_1}^2(R_\text{s} + R_\text{eq})^2 - \beta_2}{1 - k^2}\right], \quad \Psi = \sqrt{\Theta^2 + \frac{\beta_2 {\beta_1}^2 (R_\text{s} + R_\text{eq})^2}{L_\text{p}^4(1 - k^2)}}, \tag{3.8}$$

$$\beta_1 = \frac{L_\text{p}}{L_\text{s}}, \quad \beta_2 = \frac{L_\text{p}}{C_\text{p}}, \tag{3.9}$$

where their characteristics can be investigated through discriminant calculation that can be found in [30]. Any root that has a positive and real value is the ω_0. In the series-none IPT system case, multiple roots with

such a value can be avoided to prevent a frequency split at a relatively high k [14].

At the resonance, the expressions of $\mathbf{i_p}$ and $\mathbf{i_s}$ become

$$\mathbf{i_{p(res)}} = V_{eq}/\left[R_p + \frac{\omega_0^2 M^2 (R_{eq}+R_s)}{\omega_0^2 L_s^2 + (R_{eq}+R_s)^2}\right], \tag{3.10}$$

$$\mathbf{i_{s(res)}} = V_{eq}/\left\{\frac{R_p L_s}{M} + \frac{\omega_0^2 L_s M (R_s+R_{eq})}{(R_s+R_{eq})^2 + \omega_0^2 L_s^2} + j\left[\frac{\omega_0^3 L_s^2 M}{(R_s+R_{eq})^2 + \omega_0^2 L_s^2} - \frac{R_p(R_s+R_{eq}) + \omega_0^2 M^2}{\omega_0 M}\right]\right\}, \tag{3.11}$$

which are derived by inserting (3.5) into (3.2).

3.3.2 Link efficiency and voltage gain

Link efficiency is a measure indicating the effectiveness of the transfer of power between the primary and secondary sides. Since the MMCFS-IPT is operated at the ω_0, this efficiency is calculated during the resonance as

$$\eta_{link} = \frac{P_s}{P_p}, \qquad P_s = |\mathbf{i_{s(res)}}|^2 R_{eq}, \qquad P_p = V_{eq}\mathbf{i_{p(res)}}, \tag{3.12}$$

where P_s and P_p are the power consumed by R_{eq} and the primary LC circuit, respectively. The link efficiency can be further derived by inserting (3.10) and (3.11) into (3.12) as follows:

$$\eta_{link} = \frac{\left[\frac{\omega_0^2 M^2 (R_s+R_{eq})}{\omega_0^2 L_s^2 + (R_s+R_{eq})^2}\right]}{\left[R_p + \frac{\omega_0^2 M^2 (R_s+R_{eq})}{\omega_0^2 L_s^2 + (R_s+R_{eq})^2}\right]} \frac{R_{eq}}{(R_s+R_{eq})} \tag{3.13}$$

$$= \frac{\omega_0^2 M^2 R_{eq}}{\omega_0^2 M^2 (R_s+R_{eq}) + R_p\left[(R_s+R_{eq})^2 + \omega_0^2 L_s^2\right]}, \tag{3.14}$$

$$= \frac{1}{1 + \frac{1}{Q_s\gamma} + \frac{\gamma}{k^2 Q_p} + \frac{2}{k^2 Q_p Q_s} + \frac{1}{k^2 Q_p Q_s^2 \gamma} + \frac{1}{k^2 Q_p \gamma}}, \tag{3.15}$$

$$k = \frac{M}{\sqrt{L_p L_s}}, \quad Q_p = \frac{\omega_0 L_p}{R_p}, \quad Q_s = \frac{\omega_0 L_s}{R_s}, \quad \gamma = \frac{R_{eq}}{\omega_0 L_s}. \tag{3.16}$$

Primary and secondary side quality factors are denoted by Q_p and Q_s, respectively, while γ indicates the load matching factor [5].

The optimum value of R_{eq} that corresponds to the maximum value of η_{link} is derived in Publication I. Such value of R_{eq}, namely R_{opt} is expressed as

$$R_{opt} \approx \omega_0 L_s \sqrt{k^2+1}. \tag{3.17}$$

Therefore, the maximum value of η_{link} in a series-none IPT system mainly depends on ω_0, L_s and k.

In an actual stationary IPT application, variable k may change due to several reasons, such as the aging of electrical components and the position inconsistency of the primary and secondary sides. Such k variation requires continuous tuning of R_{eq} to R_{opt} to maintain the maximum value of η_{link} at steady-state operation. This tuning can be achieved using a secondary side DC-DC converter [5, 11].

Voltage gain is a ratio between V_s (the output voltage over R_{eq}) and V_{eq}, which can be expressed as follows:

$$G = \frac{V_s}{V_{eq}} = \frac{\sqrt{P_p \eta_{link} R_{eq}}}{V_{eq}} = \frac{\omega_0 M R_{eq} \sqrt{(R_{eq}+R_s)^2 + \omega_0^2 L_s^2}}{\omega_0^2 M^2 (R_{eq}+R_s) + R_p\left[(R_{eq}+R_s)^2 + \omega_0^2 L_s^2\right]}, \quad (3.18)$$

$$= \frac{\eta_{link}\sqrt{(R_{eq}+R_s)^2 + \omega_0^2 L_s^2}}{\omega_0 M} = \frac{\eta_{link}}{k}\sqrt{\frac{1}{\beta_1}\left[\left(\gamma + \frac{1}{Q_s}\right)^2 + 1\right]}. \quad (3.19)$$

3.3.3 Current damping mechanism

Under-damped behavior of $i_p(t)$ is preferred in a series-none IPT system based on ZCS. This is because such behavior prolongs the current oscillation for a certain period of time. The behavior is determined by the damping ratio of the MMCFS load in the IPT system, which is a ratio between the exponential decay frequency and the resonant frequency. This ratio is calculated from a set of dynamic equations based on the bottom schematic of Figure 3.4 as follows:

$$\begin{cases} \dot{v_{cp}}(t) = \frac{i_p(t)}{C_p}, \\ v_p(t) = v_{cp}(t) + i_p(t)R_p + L_p\dot{i_p}(t) - M\dot{i_s}(t), \\ 0 = i_s(t)(R_s + R_{eq}) + L_s\dot{i_s}(t) - M\dot{i_p}(t), \end{cases} \qquad v_p(t) = \begin{cases} \mathrm{Max}(v) & ,0 < t \le \frac{T_0}{2}, \\ 0 & ,\frac{T_0}{2} < t \le T_0, \end{cases} \quad (3.20)$$

where M was given in (2.16), $v_p(t)$ is the voltage over the primary LC network, and $v_{cp}(t)$ is the voltage over C_p.

The process to achieve the damping ratio expression of the series-none IPT system requires discriminant and dominant pole (the closest pole to the imaginary axis in a complex plane) assumptions, and involves several steps. First, the following state-space form is constructed based on (3.20):

$$\begin{bmatrix} \dot{v_{cp}}(t) \\ \dot{i_p}(t) \\ \dot{i_s}(t) \end{bmatrix} = \underbrace{\begin{bmatrix} 0 & \frac{1}{C_p} & 0 \\ -\frac{L_s}{L_pL_s - M^2} & -\frac{R_pL_s}{L_pL_s - M^2} & -\frac{M(R_s+R_{eq})}{L_pL_s - M^2} \\ -\frac{M}{L_pL_s - M^2} & -\frac{MR_p}{L_pL_s - M^2} & -\frac{L_p(R_s+R_{eq})}{L_pL_s - M^2} \end{bmatrix}}_{\mathbf{A}} \begin{bmatrix} v_{cp}(t) \\ i_p(t) \\ i_s(t) \end{bmatrix} + \begin{bmatrix} 0 \\ \frac{L_s}{L_pL_s - M^2} \\ \frac{M}{L_pL_s - M^2} \end{bmatrix} v_p(t). \quad (3.21)$$

Secondly, determinant is calculated to obtain the eigenvalues of matrix **A**:

$$|s\mathbf{I}-\mathbf{A}| = s^3 + \left[\frac{R_\mathrm{p}L_\mathrm{s}+L_\mathrm{p}(R_\mathrm{s}+R_\mathrm{eq})}{L_\mathrm{p}L_\mathrm{s}-M^2}\right]s^2 + \left[\frac{R_\mathrm{p}(R_\mathrm{s}+R_\mathrm{eq})C_\mathrm{p}+L_\mathrm{s}}{C_\mathrm{p}(L_\mathrm{p}L_\mathrm{s}-M^2)}\right]s + \frac{(R_\mathrm{s}+R_\mathrm{eq})}{C_\mathrm{p}(L_\mathrm{p}L_\mathrm{s}+M^2)}. \tag{3.22}$$

The eigenvalues are the roots of the cubic equation in (3.22), which are also the poles of the series-none IPT system [31]. Since the under-damped behavior is preferred, the system must have a pair of complex conjugate poles. Therefore, the discriminant of the cubic equation must be $D > 0$ [32]. By assuming such discriminant value is fulfilled, the poles of (3.22) become

$$s_{1,2} = -\zeta\omega_0 \pm \mathrm{j}\omega_0\sqrt{1-\zeta^2}, \qquad s_3 = c_3, \tag{3.23}$$

where ζ is the damping ratio, and c_3 is a real constant. Additionally, by assuming c_3 is sufficiently far from the real axis on the negative side, the complex conjugate poles become dominant. Under this assumption, the behavior of the cubic equation can be approximated by that of its second order part comprising the dominant poles. Finally, the ζ can be calculated as follows [14, 31, 33]:

$$\zeta = \frac{|\mathrm{Re}\{s_1\}|}{|s_1|} = \frac{|\mathrm{Re}\{s_2\}|}{|s_2|}. \tag{3.24}$$

3.4 Bi-directional power transfer of a MMCFS-based IPT system

The bi-directional power transfer capability of a MMCFS-based IPT system is explained in Publication IV, and the circuit diagram of such system is shown in Figure 3.5. The figure demonstrates that the secondary side consists of a LC network (i.e., L_s and C_s) and an active bridge topology (i.e., $\mathrm{S_{f1}}$, $\mathrm{S_{f2}}$, $\mathrm{S_{g1}}$ and $\mathrm{S_{g2}}$) connected to a voltage source $v_\mathrm{o}(t)$. The compensation configuration of this IPT system is series-series due to the existence of C_p and C_s. Both circuit sides are magnetically coupled, and their controllers communicate through a wireless communication channel.

For transferring power from the primary to the secondary (PTS) side, the IPT system only operates the MMCFS switches while utilizing the passive rectification of the diode bridge on the secondary side. Therefore, electric power flows from the three-phase voltage source to the $v_\mathrm{o}(t)$ on the secondary side. In this scenario, the current commutations and modulation strategies of the MMCFS are identical to those explained in Section 2.2.1 and 2.2.2, respectively. In the case of power transfer from the secondary to primary (STP) side, the electric power flows from $v_\mathrm{o}(t)$ to the primary circuit through an inversion process using the active bridge on the secondary side. The switches of the MMCFS are simultaneously operated to transfer this power to the three-phase input.

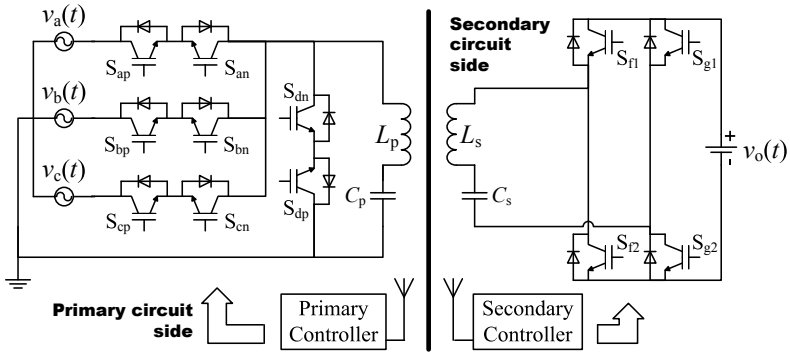

Figure 3.5. Topology of a bi-directional IPT system using MMCFS on the primary side © 2018 IEEE.

3.4.1 Current commutation in STP power transfer

On the primary side, the current commutations of the MMCFS are equal to those described in Section 2.2.1. However, $v_p(t)$ is shifted 180° with respect to $i_p(t)$. In addition, the current commutations on the secondary side are depicted in Figure 3.6, in which the flow of $i_s(t)$ are marked by bold lines. Analogous to the MMCFS, injection and FWO commutations are also applied by the bridge. In the STP case, the switching states of the bridge are described in Table 3.1 in which a value of "1" marks the on state, while "–" indicates the off state. This table shows that two modes of FWO can be used for the STP.

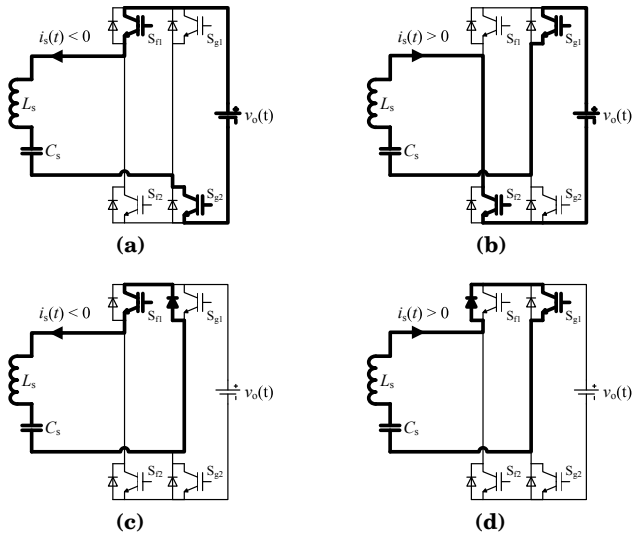

Figure 3.6. Current commutations of the full-bridge converter on the secondary side. (a) Negative injection. (b) Positive injection. (c) Negative FWO. (d) Positive FWO.

Table 3.1. Switching states of secondary-side converter

	$i_s(t) < 0$				$i_s(t) > 0$			
	S_{f1}	S_{f2}	S_{g1}	S_{g2}	S_{f1}	S_{f2}	S_{g1}	S_{g2}
Injection	1	–	–	1	–	1	1	–
FWO (1)	1	–	–	–	–	–	1	–
FWO (2)	–	–	–	1	–	1	–	–

3.4.2 Modulation of secondary-side converter

For STP, a PDM similar to that of NIM and SIM is used in the inversion process of the bridge converter, thus power flow is also regulated by varying the number of injections with respect to FWOs. The modulation process is illustrated in Figure 3.7, in which injections are marked by bars with diagonal stripes and FWOs are indicated by zero on the time axis. In this modulation, the injection source is $v_o(t)$, which has an amplitude of V_o. Analogous to NIM and SIM, transition between the commutations is performed at zero-crossing of $i_s(t)$. This type of modulation is similar to the square-wave operation using unipolar and bipolar voltage switchings described in [15].

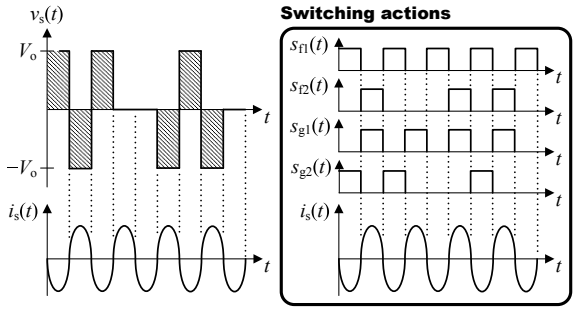

Figure 3.7. The modulation of inversion process with controlled power flow © 2018 IEEE.

4. Implementation and Data Analysis

This chapter analyzes ideal and actual system behaviors. Section 4.1 presents the simulation results of MMCFS-based IPT systems. These results contain both unidirectional and bi-directional power transfer operations. Section 4.2 describes an actual prototype of the series-none MMCFS-IPT system. This section also elaborates the electrical and electronic components used in the actual prototype as well as practical requirements (e.g., a kick-start method and a multistep strategy). Finally, the experimental data of the prototype are analyzed and compared with theoretical calculations in the last section of this chapter.

4.1 Ideal System Characteristics

The operations of MMCFS-IPT are demonstrated at the simulation level, in which the electrical components of the IPT system are assumed to be ideal. In both unidirectional and bi-directional power transfer cases, the simulation is configured for maximum output power operation. As a result, the varying sparseness of injections is not demonstrated. The electrical parameters of the MMCFS-IPT in this ideal condition are shown in Table 4.1, where f_l denotes the line input frequency in Hertz. The parameter values were chosen based on the damping ratio and the resonant frequency of the LC-L and equivalent AC load. These values do not conform to a standard for a certain application.

Table 4.1. Ideal system parameters

f_l (Hz)	C_p (nF)	L_p (μH)	R_p (Ω)	C_s (nF)*	L_s (μH)	R_s (Ω)
50	200	200	0.3	200	200	0.3

*Capacitor C_s is only used in bi-directional power transfer simulation.

4.1.1 Unidirectional power transfer operation

In the unidirectional power transfer case, the LC-L network and load configurations are based on the bottom schematic of Figure 3.4. The V_{amp} of the input three-phase was set to 100 V, the k of the coupled coil was fixed to 0.55 and R_{eq} was set to 38.698 Ω. This resistance value is the R_{opt} (see Section 3.3.2) for the given parameters in Table 4.1, and was calculated in Publication I.

The voltage and current waveforms of NIM and SIM operations are presented in Figure 4.1, which are based on Publication V. From the input voltage graphs, NIM uses only one input phase (in this case Phase A) for performing injection, while in contrast, SIM utilizes two input phases (in this case Phase A and Phase C). Consequently, the current amplitudes of SIM are larger than those of NIM.

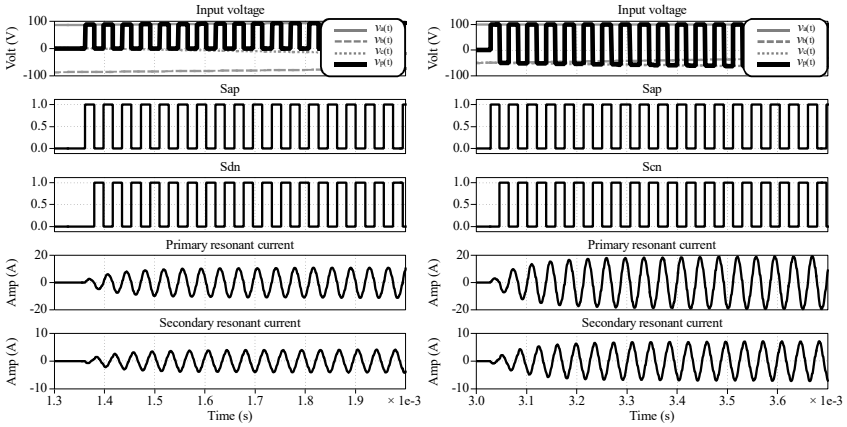

Figure 4.1. Simulation results of unidirectional power transfer operation. (a) NIM utilizing Sap and Sdn switches. (b) SIM utilizing Sap and Scn switches.

The extracted electrical quantities of voltages and currents in Figure 4.1 at steady-state are presented in Table 4.2. These values are based on the resonance operating point, which is 26.835 kHz. The ratios of $V_{\text{sim(M)}}/V_{\text{nim(M)}}$ and $P_{\text{sim(M)}}/P_{\text{nim(M)}}$ are approximately 1.626 and 2.643, respectively. The first ratio was obtained by dividing V_{p} of SIM by that of NIM, while the second ratio was calculated by dividing P_{p} of SIM by that of NIM from the Table 4.2. These ratios are in close agreement with the theoretical predictions outlined in Section 2.2.2.

Table 4.2. Electrical quantities at the resonant frequency

	V_{p} (V_{rms})	I_{p} (A_{rms})	I_{s} (A_{rms})	P_{p} (W)
NIM	39.036	7.29	2.622	284.541
SIM	63.458	11.849	4.263	751.922

4.1.2 Bi-directional power transfer operation

The application of MMCFS-IPT for bi-directional power transfer is explained in Publication IV. In this case, the simulation model is based on the schematic provided in Figure 3.5. The configuration has a three-phase amplitude of 230 V, $k = 0.1$ and $V_o = 388.2\ V$. The amplitude of $v_o(t)$ (V_o) on the secondary side was chosen to produce $V_s = 2.5V_p$.

Primary to secondary power transfer
Simulated waveforms of PTS power transfer are shown in Figure 4.2. The MMCFS switching frequency is approximately $158.291 \cdot 10^3$ rad/s or 25.193 kHz, and the average power on the input side is $15.897 \cdot 10^3$ W.

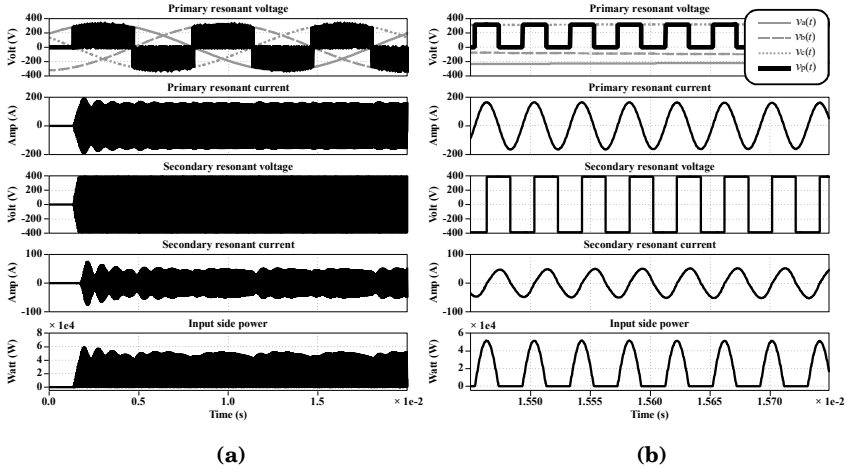

Figure 4.2. Simulation results of PTS power transfer, in which (b) is the magnification of (a) on the time axis © 2018 IEEE.

Secondary to primary power transfer
In STP power transfer, the simulation waveforms are shown in Figure 4.3. In this case, the phase difference between the voltage and current in both primary and secondary sides is 180°, as can be seen in Figure 4.3(b). The MMCFS switching frequency is approximately $166.53 \cdot 10^3$ rad/s or 26.504 kHz, and the average power on the input side is $-48.89 \cdot 10^3$ W.

4.2 Experimental setup

The experimental setup of a series-none MMCFS-IPT system is shown in Figure 4.4. Each printed circuit board (PCB) in MMCFS of the IPT system was designed by the author of this dissertation, and the board manufacturing process was outsourced from a private PCB company. The entire circuit was built in a modular form with multiple test points for

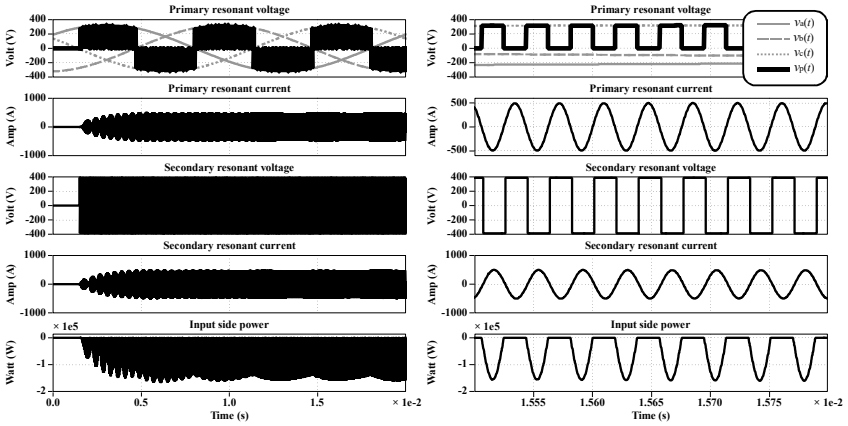

Figure 4.3. Simulation results of STP power transfer, in which (b) is the magnification of (a) on the time axis © 2018 IEEE.

debugging purposes.

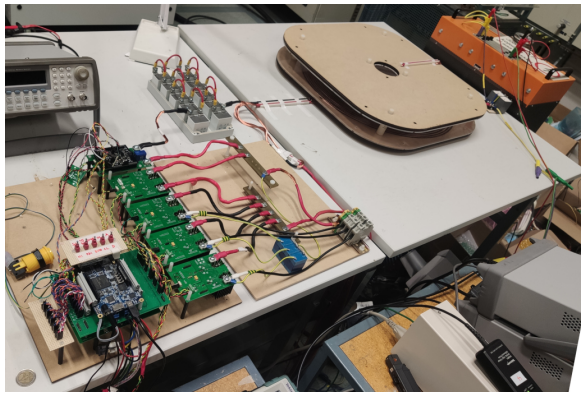

Figure 4.4. The experimental setup of a series-none MMCFS-IPT system.

Figure 4.5 depicts a general block diagram of the IPT system in which thick arrows indicate power flow, whereas thin arrows mark control signals. The three-phase voltage is a programmable AC power source (i.e., Regatron TC50.480.72-ACS-14026). The source is connected to three input capacitors to reduce the influence of the input line inductance. Each input capacitor (i.e., Epcos 12 μF) is connected in parallel between one input phase and a neutral. The switching network comprising eight discrete IGBTs (i.e., Infineon IKW40N120H3) is attached between the input capacitors and the primary capacitor C_{p}. The C_{p} was built by connecting ten 2 μF film capacitors (i.e., KEMET C4B MKP) in series. The coupled coil is connected between the capacitor bank and the AC load. This AC load represents the components in the gray area in Figure 3.4, which consists

of a full-bridge rectifier (i.e., SemiQ GHXS030A060S-D1E), a smoothing film capacitor of 66 μF, and a variable resisitive load (i.e., Terco MV1100).

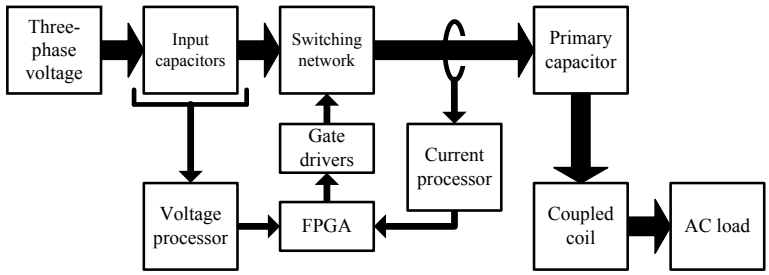

Figure 4.5. The block diagram of a series-none MMCFS-IPT system.

Figure 4.5 also displays a voltage processor being used to determine a phase of the input voltage. This processor employs resistor dividers as well as a phase-locked loop circuit. Additionally, the current processor is used to monitor amplitude and zero-crossing of $i_{\mathrm{p}}(t)$. This current processor consists of a current transducer (i.e., LEM CASR-6), a precision rectifier, and a ZCD circuit. A field-programmable gate array (FPGA) circuit (i.e Terasic DE10-Nano) is used to perform a modulation method, which involves logic operations and utilizes the outputs of both voltage and current processors. This modulation produces gate signals to control the switching network. The gate drivers (i.e., Texas Instruments UCC21521) convert these signals to suitable voltages for switching IGBTs in the switching network. Each driver is powered by an isolated power supply (i.e., CUI VQA-S15-D15-SIP). The gate resistances for turning-on and turning-off the IGBTs have a value of 10 Ω, which were randomly selected from the IGBT manufacturer's datasheet.

4.2.1 Coil configuration

To simplify the coil manufacturing process, a flat spiral coil with an air core was chosen for the series-none MMCFS-IPT setup. The coil dimensions were calculated using the Wheeler approximation formula to achieve a self-inductance of 200 μH [34, 35]. Both primary and secondary coils were constructed from a litz wire that contains 1000 strands of 38 gauge (i.e., American wire gauge) isolated wire to reduce the skin effect. The number of strands and gauge size were selected based on the $i_{\mathrm{p}}(t)$ requirement and the ω_0 of the IPT system, respectively. A supporting platform for each coil was built from plywood and plexiglass materials, which were cut using a laser cutter in the Aalto Fablab. Each coil was manually assembled by hand.

The illustration and dimensions of the single coil are provided in Figure 4.6. Additionally, an illustration of coupled coil consisting of L_{p} and L_{s} in the experimental setup is shown in Figure 4.7. In the setup, both L_{p} and

L_s are placed facing each other at a distance of d_c with no misalignment. The coil design is not optimized since it is not the focus of this dissertation.

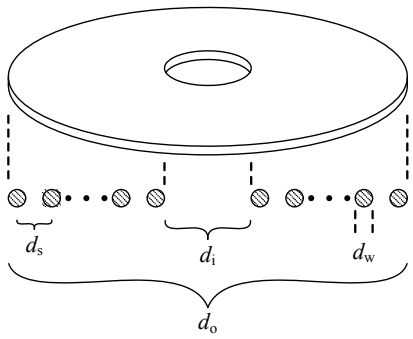

Symbol	Meaning	Value
d_i	Inner diameter	163 mm
d_o	Outer diameter	532 mm
d_s	Wire separation	3 mm
d_w	Wire diameter	4.7 mm
N_t	Number of turns	24

Figure 4.6. Diagonal and lateral illustrations of a single IPT coil. Circles with diagonal stripes represent the wire cross section.

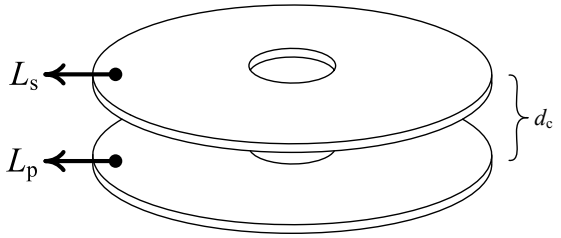

Figure 4.7. Diagonal view of the primary and secondary coils in a practical application.

4.2.2 Practical passive component values

In practice, passive components forming the LC-L network have a degree of accuracy and contain parasitic elements. Therefore, it is beneficial to measure the actual values of the components using a RCL meter and a multimeter. In addition, to calculate the mutual inductance of L_p and L_s, a series-connected measurement is required as can be seen in Figure 4.8. In this figure, the measurement current is denoted by $i_m(t)$ and each coil polarity is marked by a dot. The series measurement using opposite and identical polarities produces two additional inductances, namely L_1 and L_2 [26]. Thus, the mutual inductance of the coupled L_p and L_s can be obtained by the following equation:

$$M = \frac{L_1 - L_2}{4}. \tag{4.1}$$

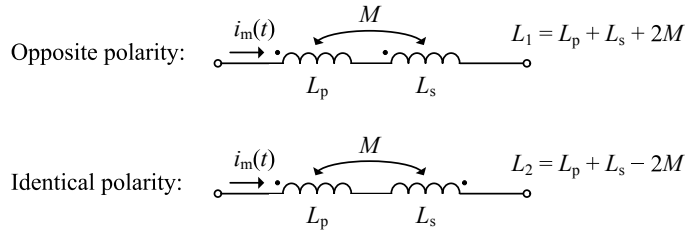

Figure 4.8. Two connection types of L_p and L_s for M calculation.

4.2.3 Kick-start method

A kick-start method is elaborated in Publications III and VI. Since the MMCFS in the IPT system uses a modulation strategy based on ZCS, an oscillating current in the LC-L circuit is needed at the initial stage for triggering a steady-state operation. This kick-start method charges C_p to a certain voltage level, then release the accumulated energy in the capacitor using the free-wheeling switch of the MMCFS. To charge the capacitor, an approach based on the DC resonant charging is used by benefiting from the series-none MMCFS-IPT topology. Figure 4.9 shows a current injection path extracted from the MMCFS-IPT schematic, which resembles the DC resonant charging circuit. Since the MMCFS has three input channels, the converter can charge the capacitor from three different sources.

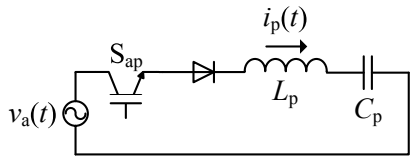

Figure 4.9. Injection path of the series-none MMCFS-IPT using Phase A.

The injection sequence of the charging process is illustrated in Figure 4.10. The figure shows that the switching network of the MMCFS generates pulses of positive and negative voltages sequentially from three different inputs at the beginning of Max(v) regions. These applied pulses with a duration grater than $T_0/2$ increase the capacitor voltage (i.e., $v_{cp}(t)$) and energy to certain levels. When this energy is released by the MMCFS-IPT free-wheeling switch, an oscillating current in the primary LC circuit is produced. The amplitude of this current is directly proportional to the final charging voltage of the capacitor, which can be calculated using the dynamic equation provided in Publication III.

The steady-state operation of the MMCFS-IPT can be triggered at different combinations of input voltage amplitude, coupling factor and load condition using the kick-start method.

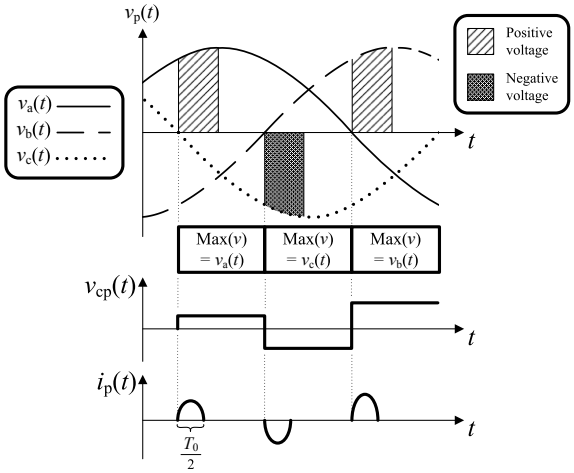

Figure 4.10. Injection voltage sequence of $v_p(t)$ in the kick-start process.

4.2.4 Multistep switching

A practical semiconductor device with three-terminal configuration is not an ideal switch due to parasitic elements. As a result, actual switching transition in a power converter is not instantaneous. To overcome this limitation, a multistep switching strategy based on current zero-crossing was developed for operating the MMCFS switching network. This strategy allows the converter to use the non-ideal switch while simultaneously preventing two switching prohibitions described in Section 2.1.2. However, this approach prevents the actual MMCFS from performing the ZCS operation.

The multistep switching strategy for positive and negative injections from Phase A is illustrated in Figure 4.11. The variable T_d denotes the injection duration and T_b denotes the blanking time. Both time variables must be chosen to ensure a continuous oscillation of $i_p(t)$ in the IPT system. Additionally, T_{asc} and T_{des} denote delays of the Sap signal with respect to $i_p(t) = 0$. Similarly, the same switching transitions can also be applied to injections from Phases B and C.

The non-ideality of the semiconductor device and the implementation of the multistep switching strategy in the MMCFS affect the input voltage approximation provided in Section 2.2.2. As a result, corrections are required to accommodate the influence. For NIM, the corrected version of (2.7) is explained in Publication VI, which has a form of

$$V_{mag} \approx 2V_{corr}\left[\sum_{k_1=0}^{k_1=(N_1-1)} \sin\left(\omega_l\left[k_1\frac{T_0}{2}+T_{asc}\right]+\frac{\pi}{3}\right)\right]\frac{T_{corr}}{T_t}, \tag{4.2}$$

$$V_{corr} = V_{amp} - V_{dt} - V_{dd}, \quad T_{corr} = \frac{T_0}{2} - T_{asc} - T_{des}. \tag{4.3}$$

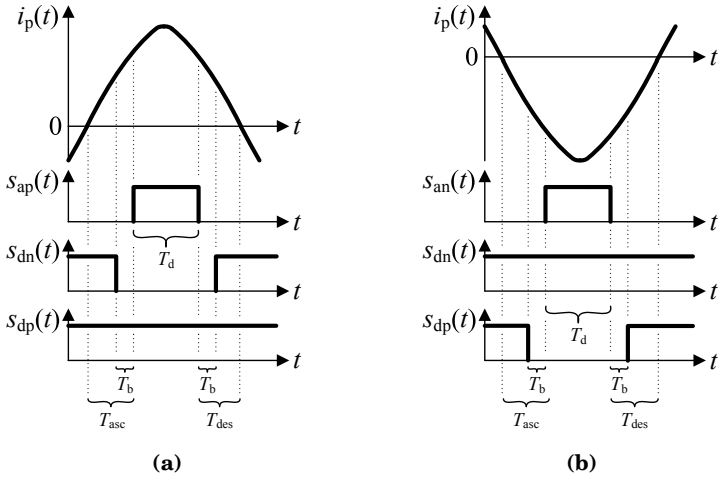

Figure 4.11. Multistep switching strategy. (a) Positive injection case. (b) Negative injection case.

The V_{dt} and V_{dd} denote corrections due to the voltage drops of IGBT and its own anti-parallel diode, respectively.

4.2.5 Zero-crossing detector circuit

In the context of MMCFS, a ZCD circuit approximates zero crossing of $i_p(t)$ corrupted with Gaussian noise for assisting the FPGA controller to produce gate signals. The ZCD circuit used in the experimental setup of a series-none MMCFS-IPT system are described in Publication II. The circuit diagram and voltage characteristics of this ZCD are shown in Figure 4.12 and Figure 4.13, respectively. The circuit is composed of a passive low-pass filter constructed by R_f and C_f, a dynamic hysteresis comparator (DHC), and an edge-triggering circuit. The detection process of the zero crossing involves several steps: conversion of $i_p(t)$ to $v_{dis}(t)$ by a current transducer (i.e., LEM CASR-6), partial filtering of $v_{dis}(t)$ to produce $v_{fo}(t)$, polarity marking of $v_{fo}(t)$ by the DHC using square voltage $v_{co}(t)$, and zero crossing marking by the edge-triggering circuit using $v_z(t)$. In the prototype of the series-none MMCFS-IPT system, this edge-triggering circuit is implemented in the FPGA.

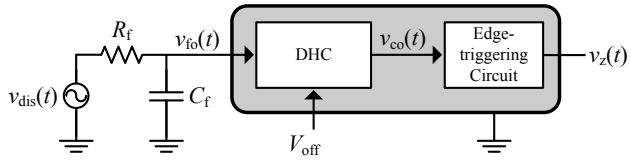

Figure 4.12. ZCD circuit diagram © 2017 IEEE.

The DHC circuit is an essential component of the ZCD. The schematic and voltage waveforms of such a circuit are presented in Figure 4.14, which

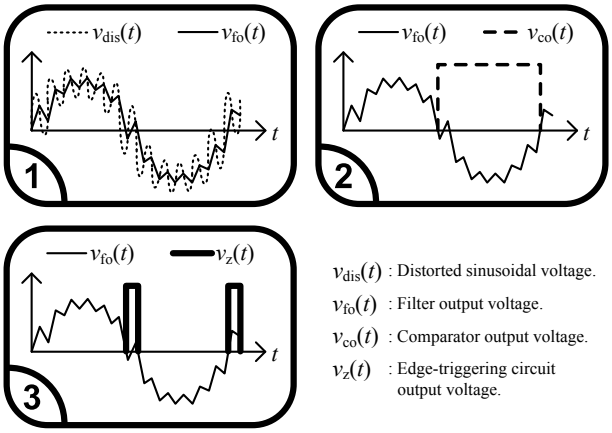

Figure 4.13. The voltage characteristics of ZCD circuit © 2017 IEEE.

displays that the circuit is formed by combining an op-amp and a passive differentiator consisting of C_d and R_d. The input signal $v_{fo}(t)$ is expected to be sinusoidal with a period of T_{fo}, and may have DC offset. In the MMCFS-IPT application, the period is equal to the resonant frequency period (i.e., T_0). The differentiator transforms square voltage $v_{co}(t)$ to decaying voltage $v_h(t)$ that is used as hysteresis by the op-amp. The decay time of $v_h(t)$ depends on the values of C_d and R_d, whereas the offset of $v_h(t)$ is determined by V_{off}. Since this offset shifts the peak of $v_h(t)$ to V_{tot}, the op-amp input must be able to handle such voltage increment. Note that the V_{off} in Figure 4.14 is the same as that of Figure 4.12.

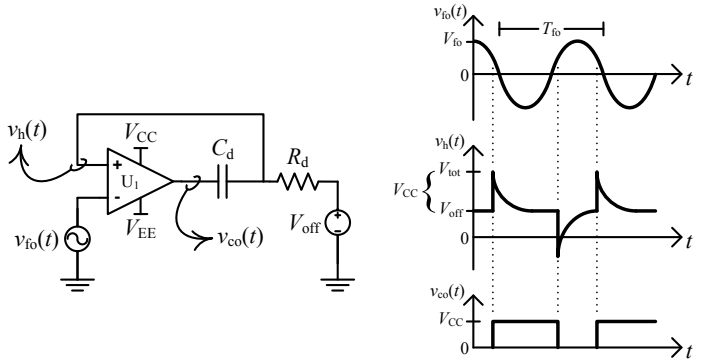

Figure 4.14. Schematic and voltage waveforms of the DHC circuit © 2017 IEEE.

For a ZCD application in MMCFS-IPT systems, V_{off} must be identical to the offset of $v_{fo}(t)$. In addition, the decay time of $v_h(t)$ must be slightly lower than $T_{fo}/2$ to prevent the lagging of $v_{co}(t)$. In the actual prototype of the series-none MMCFS-IPT system, the LT1711 from Analog Devices is used as the op-amp.

4.3 MMCFS-IPT Data Analysis

The behavior of an actual series-none MMCFS-IPT system is analyzed by comparing theoretical calculations and experimental data. The analysis presented in this section is adapted from Publication VI and limited to the case of unidirectional power transfer in which MMCFS is driven by NIM. The electrical quantities of the actual IPT system and its auxiliary circuits are provided in Table 4.3. These values were measured by the Fluke 28-II multimeter and the PM6306 RCL meter. In the ZCD and DHC table, the quantities originate from the nominal values of the components. Since the sinusoidal input of the ZCD (i.e., CASR-6 output) is shifted by 2.5 V, the V_{off} of the DHC is supplied by the same voltage level using the LM4030 voltage reference from Texas Instruments.

Table 4.3. Actual electrical characteristics

MMCFS-IPT:

V_{amp} (V_{rms})	f_{l} (Hz)	C_{p} (nF)	L_{p} (μH)	R_{p} (Ω)	L_{s} (μH)	R_{s} (Ω)	C_{L} (μF)	R_{L} (Ω)	d_{c} (cm)	k -
70.8	50	203.7	196.7	0.08	196	0.1	66	49.9	5.5	0.53

ZCD and DHC:

R_{f} (Ω)	C_{f} (pF)	R_{d} (Ω)	C_{d} (nF)	V_{CC} (V)	V_{EE} (V)	V_{off} (V)
$51 \pm 0.1\%$	$220 \pm 5\%$	$231 \pm 0.1\%$	$4.7 \pm 10\%$	5	-5	2.5

Experimental data for visualization purpose were measured and recorded using two oscilloscopes (i.e., Tektronix TPS 2024B and TPS 2014B). These data were then re-plotted by MATLAB for clarity. Additionally, the Tektronix MDO4104C oscilloscope were used to measure and record high resolution waveforms for data extraction.

4.3.1 Coupling factor limitation

The eigenvalues plot of the actual series-none MMCFS-IPT system is shown in Figure 4.15, which is based on the parameters provided in Table 4.3. In addition, the calculated values of D and ζ with respect to different k numbers are shown in a table under the graph. The table reveals that high k corresponds to high ζ, which can shorten the free-wheeling duration of $i_{\text{p}}(t)$ oscillation. Consequently, the timespan of successive FWOs becomes limited for the continuous operation of the IPT system.

4.3.2 Practical kick-start process

The waveforms of the actual MMCFS-IPT system during the kick-start process are presented in Figure 4.16. As can be seen from the plot of

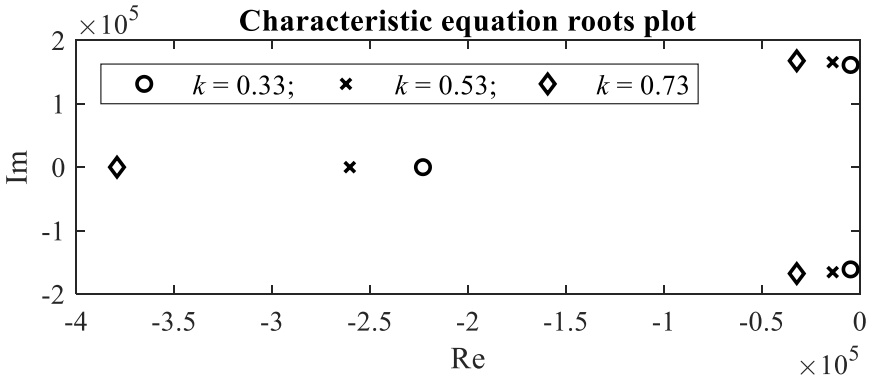

	k		
	0.33	0.53	0.73
D	$5.21 \cdot 10^{30}$	$7.88 \cdot 10^{30}$	$2.3 \cdot 10^{31}$
ζ	0.03	0.08	0.19

Figure 4.15. The plot of eigenvalues with respect to k and their corresponding D and ζ.

$v_{\mathrm{p}}(t)$, three injections were utilized to charge the voltage over C_{p} to a level around 500 V. The accumulated energy in the capacitor is then released at 0 ms to trigger the steady-state operation. The current swell of $i_{\mathrm{p}}(t)$ at the beginning of the steady state is due to the charging process of an empty C_{L} on the load side.

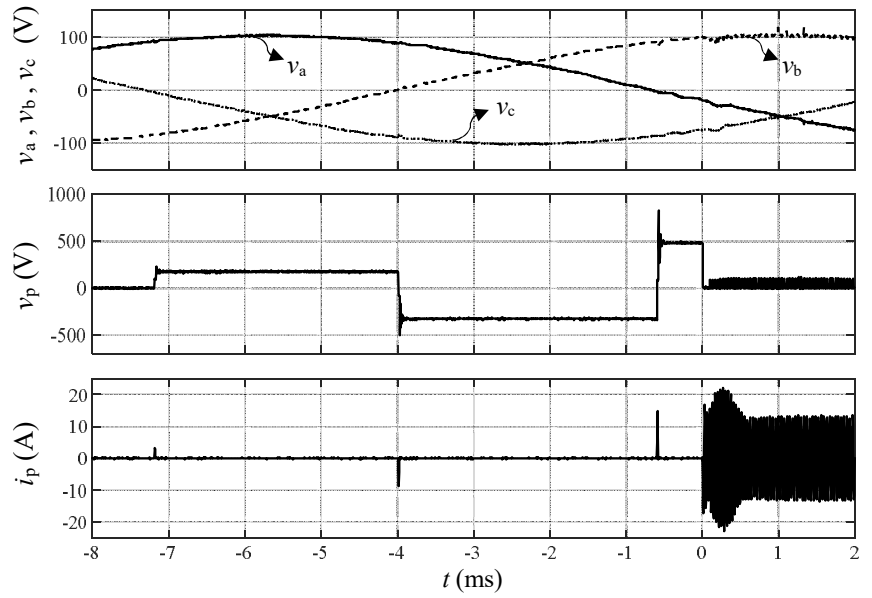

Figure 4.16. The experimental waveforms of kick-start process during which injections are performed sequentially from Phase A, C, and B.

4.3.3 Maximum output power operation

In terms of maximum output power operation, the experimental waveforms of the actual series-none MMCFS-IPT system during steady state are presented in Figure 4.17. The left half of this figure has a longer time scale than the other half. In the figure, circuit impedance causes a time-shift between $i_{\mathrm{p}}(t)$ and $i_{\mathrm{s}}(t)$ with a value of around 12.6 μs. In addition, the frequency domain plots of voltage and current in Figure 4.17 can be seen in Figure 4.18, which were calculated using the fast Fourier transform. The y-axis of each plot marks the peak value of frequency components. In these plots, there is only one frequency component that yields the largest contribution to power transfer, which is 26.675 kHz. This frequency is the switching frequency of the MMCFS-IPT system, which is equal to the ω_0 of the series-none IPT system.

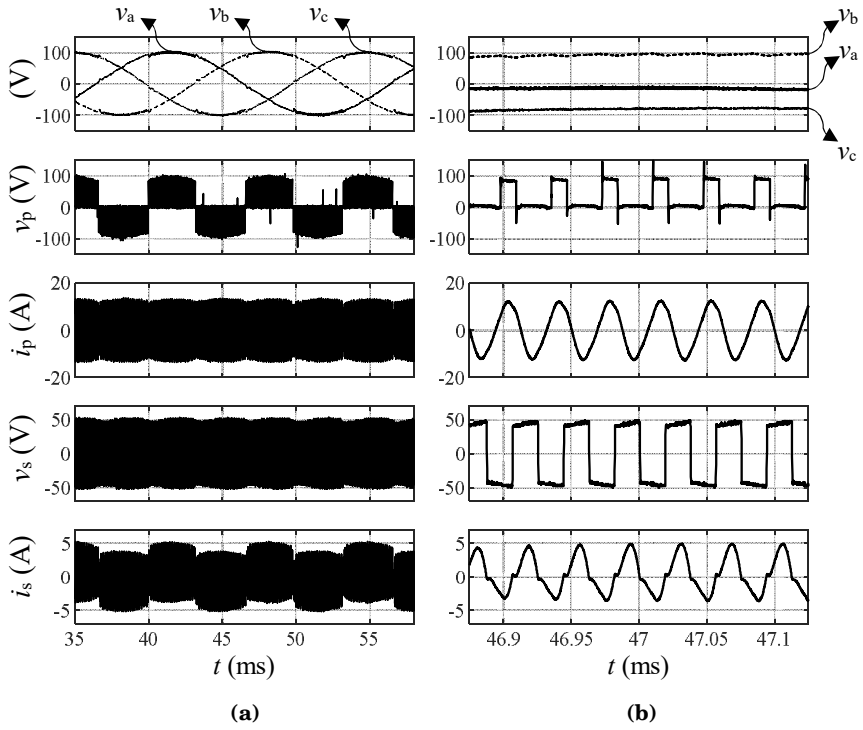

Figure 4.17. The electrical waveforms of the series-none MMCFS-IPT system using NIM. (a) Long time scale. (b) Short time scale.

Multistep switching transitions of the actual series-none MMCFS-IPT using NIM are presented in Figure 4.19. Although this figure only shows the switching transitions of positive injection from Phase A, these transitions are also valid for injection using input switches connected to Phase B or C. To prevent short circuit of the actual MMCFS, s_{ap} and s_{dn} must not conduct at the same time, therefore T_{b} was applied with a duration of 1.1 μs. Since

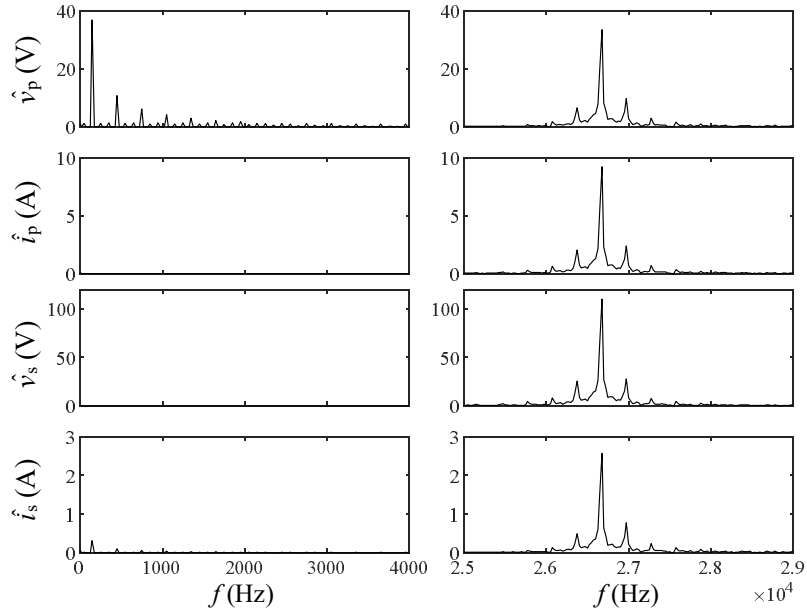

Figure 4.18. The frequency spectra of the MMCFS-IPT system waveforms. Two separate frequency axes are used to highlight dominant amplitudes.

T_d value is fixed in the prototype, the IPT system cannot accommodate variable-frequency operation. From the characteristics table adjacent to the figure, R_g denotes gate resistance in turn-on and turn-off cases. The other variables in the table were previously described in Section 4.2.4.

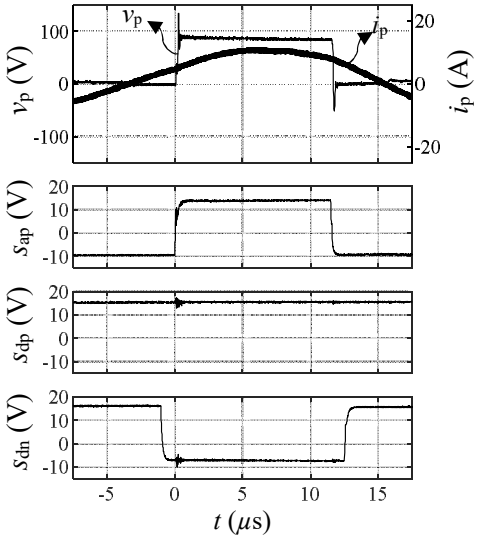

Characteristics:

R_g (Ω)	10
t_{asc} (μs)	3.5
t_{des} (μs)	3.9
t_b (μs)	1.1
t_d (μs)	11.6

Figure 4.19. Switching transitions of MMCFS during positive injection of NIM.

Theoretical calculations (Calc.) and experimental data (Exp.) are presented side by side in Table 4.4. Variable f_0 in this table is the resonant

frequency of the series-none IPT system in Hertz. As can be seen in the table, the electrical characteristics of the actual IPT system can be approximated by the theoretical models given in Chapters 2 and 3. The discrepancy between theoretical and experimental results can be attributed to an approximation error and limited measurement accuracy. Nevertheless, the overall system efficiency, which is measured from the input three-phase to the resistive load R_{L} is approximately 81.68 %.

Table 4.4. Electrical parameters from calculation and experimental results

	V_{eq} ($\mathrm{V_{rms}}$)	I_{p} ($\mathrm{A_{rms}}$)	P_{p} (W)	f_0 (kHz)	V_{s} ($\mathrm{V_{rms}}$)	I_{s} ($\mathrm{A_{rms}}$)	P_{s} (W)	η_{link} (%)	G
Calc.	24.96	5.42	135.18	26.671	73.21	1.81	132.5	98.02	2.93
Exp.	23.72	6.53	154.81	26.675	78.39	1.82	142.95	92.34	3.31

Since the corrections that were presented in Section 4.2.4 were used to calculate v_{p} in Table 4.4, voltage drops of the IGBT and its own anti-parallel diode (i.e., V_{dt} and V_{dd}) were needed. The V_{dt} and V_{dd} in this case are 1.52 V and 1.78 V, respectively, which were estimated from the IGBT manufacturer's datasheet using the collector current amplitude and junction temperature of the IGBT. The amplitude and temperature were 10 A and 25° C, respectively, which are the approximated values from the MDO4104C oscilloscope and a thermal camera (i.e., Fluke Ti110) closest to those available in the datasheet.

In the IPT system, a high voltage gain corresponds to the low amplitude of circulating current in the secondary coil, which can lead to low power loss in the coil [36].

4.3.4 Partial load operation

The partial load operation of the actual series-none MMCFS-IPT system using NIM was implemented by applying the on-off current control explained in Section 3.2.1. The experimental waveforms of such an operation are provided in Figure 4.20. Additionally, electrical quantities extracted from the waveforms are presented in Table 4.5. In this mode of operation, the number of injections and FWOs are adjusted automatically to limit I_{p} to around 6 $\mathrm{A_{rms}}$. Consequently, the average power transferred to the load on the secondary side is lower than that of the maximum output case. The overall efficiency in this particular case is 79.23 %.

Table 4.5. The electrical characteristics of the actual MMCFS-IPT system using NIM and on-off control

V_{eq} ($\mathrm{V_{rms}}$)	I_{p} ($\mathrm{A_{rms}}$)	P_{p} (W)	V_{s} ($\mathrm{V_{rms}}$)	I_{s} ($\mathrm{A_{rms}}$)	P_{s} (W)
12.76	5.74	117.5	72.04	1.9	102.16

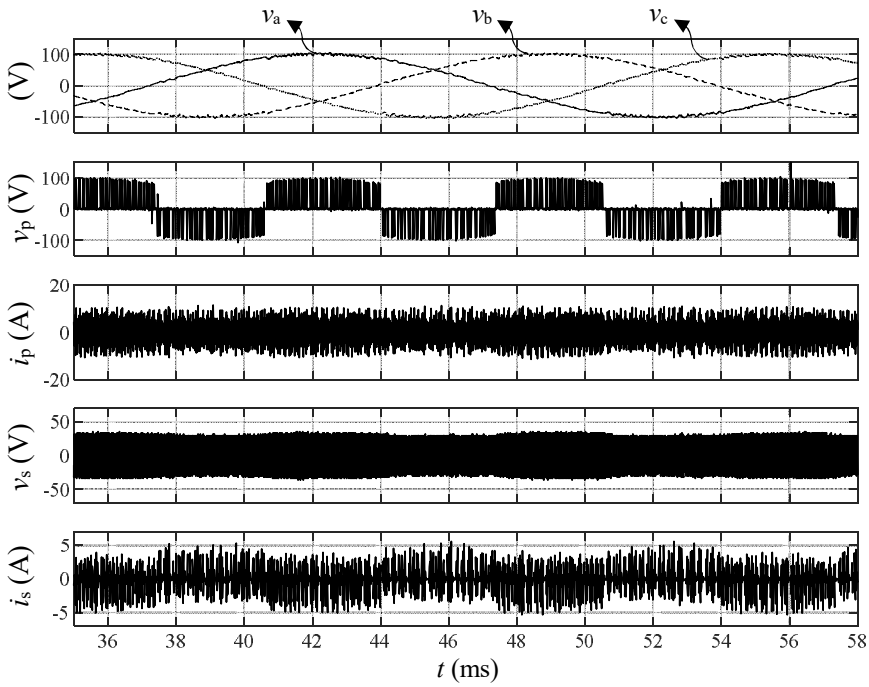

Figure 4.20. An on-off control implementation of the actual MMCFS-IPT system.

In partial load operation, the control accuracy is determined by the total number of injections within the Max(v) region. Therefore, the accuracy depends on the value of f_0. In other words, the higher the frequency, the higher the accuracy. Since the free-wheeling duration of $i_p(t)$ is short at high k, a long sequence of FWOs must be avoided to prevent an abrupt stoppage of the MMCFS-IPT operation in a steady-state condition.

5. Conclusion and Future Work

This last chapter concludes the MMCFS-IPT research presented in this dissertation. It also provides some additional findings, as well as recommends areas for further investigation.

5.1 Conclusion

This dissertation has presented research on MMCFS and its application in an IPT system. The proposed converter can be used as an alternative to the RI or VB2B topology, for reducing system complexity, size and cost. To predict MMCFS-IPT behavior, mathematical models and computer simulations were developed based on an ideal configuration. Additionally, an experimental setup was built to demonstrate the capability of the MMCFS in power conversion, as well as to validate results of the ideal approach. The outcomes of both the ideal and practical approaches are in close agreement with each other.

The research produces multiple contributions in the area of direct converter and IPT systems:

- It presents two approaches for combining PDM and MMCFS, namely NIM and SIM, based on either a maximum or minimum absolute value, respectively.
- It derives an equivalent voltage for the two proposed modulations using power equality analysis. This voltage derivation approach can also be applied to other types of ZCS-based PDM operations.
- It presents a bi-directional power transfer capability for a series-series MMCFS-IPT configuration at the simulation level.
- It introduces three practical requirements for implementing an actual series-none IPT system based on the MMCFS: a kick-start method, a multistep switching method, and a zero-crossing detector circuit.

- It describes the characteristics of the PDM-based series-none IPT system based on dynamic and steady-state mathematical models. These characteristics include damping behavior, resonant frequency, voltage and current amplitudes, as well as link efficiency and voltage gain.

In high k and quality factors application, the series-none configuration simplifies the secondary side of an IPT system, due to the absence of a secondary side compensation capacitor. Since the series-none configuration is not restricted by frequency split, it allows a self-oscillating operation with PDM to be applied to the IPT system.

In practice, using a rectifier and a smoothing capacitor on the load may eliminate the need for the kick-start method based on the DC resonant charging principle, since a single injection may produce a readable initial amplitude of $i_{\mathrm{p}}(t)$, as a consequence of the empty smoothing capacitor. In regard to multistep switching, the blanking time T_{b} is determined by the type of material used in the semiconductor switch for the MMCFS. Therefore, a wide-bandgap semiconductor, such as silicon carbide and gallium nitride can accommodate a higher value of f_0 than would be feasible when using a silicon product. Additionally, the operation of MMCFS-IPT with varying k would require a more accurate ZCD than the one developed in this dissertation.

5.2 Future Work

Due to time constraints, it was not possible to use the developed MMCFS-IPT prototype for validating all of the theoretical calculations and simulation results related to SIM operation and the bi-directional power transfer. Therefore, future work should focus on developing software and hardware for implementing these two operations in the prototype. For SIM, attention should be devoted to investigating the transient period occuring at the beginning of a steady-state operation, since the primary circuit current may increase beyond the current rating of the IGBT when charging the empty smoothing capacitor with successive injections.

A further extension of this research could include analyzing the harmonics and neutral current of the MMCFS. When the converter is connected to a utility supply, it must follow strict harmonics guidelines. Thus, the device may require a sophisticated input filter design to suppress the harmonics in its three-phase input. In addition, to avoid overloading of a nearby transformer, it is imperative that a neutral line DC current must not be produced by the MMCFS-IPT system during a steady-state operation. Unfortunately, it was not possible to analyze the DC current when the prototype was connected to the Regatron power supply. This was due to the existence of another DC current in the prototype.

References

[1] K. van Schuylenbergh and R. Puers. *Inductive Powering: Basic Theory and Application to Biomedical Systems*. Springer Netherlands, 2009.

[2] H. L. Li, A. P. Hu, and G. A. Covic. A Direct AC–AC Converter for Inductive Power-Transfer Systems. *IEEE Transactions on Power Electronics*, 27(2):661–668, 2012.

[3] M. P. Kazmierkowski and A. J. Moradewicz. Unplugged But Connected: Review of Contactless Energy Transfer Systems. *IEEE Industrial Electronics Magazine*, 6(4):47–55, 2012.

[4] S. Lukic and Z. Pantic. Cutting the Cord: Static and Dynamic Inductive Wireless Charging of Electric Vehicles. *IEEE Electrification Magazine*, 1(1):57–64, 2013.

[5] R. Bosshard, J. W. Kolar, J. Mühlethaler, I. Stevanović, B. Wunsch, and F. Canales. Modeling and η-α-Pareto Optimization of Inductive Power Transfer Coils for Electric Vehicles. *IEEE Journal of Emerging and Selected Topics in Power Electronics*, 3(1):50–64, 2015.

[6] F. P. Kusumah, S. Vuorsalo, and J. Kyyra. A direct three-phase to single-phase ac/ac converter for contactless electric vehicle charger. In *2015 17th European Conference on Power Electronics and Applications (EPE'15 ECCE-Europe)*, pages 1–10, 2015.

[7] N. X. Bac, D. M. Vilathgamuwa, and U. K. Madawala. A matrix converter based Inductive Power Transfer system. In *2012 10th International Power Energy Conference (IPEC)*, pages 509–514, 2012.

[8] N. Xuan Bac, D. M. Vilathgamuwa, and U. K. Madawala. A SiC-Based Matrix Converter Topology for Inductive Power Transfer System. *IEEE Transactions on Power Electronics*, 29(8):4029–4038, 2014.

[9] S. Weerasinghe, U. K. Madawala, and D. J. Thrimawithana. A Matrix Converter-Based Bidirectional Contactless Grid Interface. *IEEE Transactions on Power Electronics*, 32(3):1755–1766, 2017.

[10] Y. Zhang, T. Kan, Z. Yan, Y. Mao, Z. Wu, and C. C. Mi. Modeling and analysis of series-none compensation for wireless power transfer systems with a strong coupling. *IEEE Transactions on Power Electronics*, 34(2):1209–1215, 2019.

[11] J. Tritschler, B. Goeldi, S. Reichert, and G. Griepentrog. Comparison of different control strategies for series-series compensated inductive power transmission systems. In *2015 17th European Conference on Power Electronics and Applications (EPE'15 ECCE-Europe)*, pages 1–8, 2015.

[12] H. L. Li, A. P. Hu, and G. A. Covic. FPGA controlled high frequency resonant converter for contactless power transfer. In *2008 IEEE Power Electronics Specialists Conference*, pages 3642–3647, 2008.

[13] V. Esteve, E. Sanchis-Kilders, J. Jordan, E. J. Dede, C. Cases, E. Maset, J. B. Ejea, and A. Ferreres. Improving the Efficiency of IGBT Series-Resonant Inverters Using Pulse Density Modulation. *IEEE Transactions on Industrial Electronics*, 58(3):979–987, 2011.

[14] F. P. Kusumah, S. Vuorsalo, and J. Kyyrä. Components selection of a direct three-phase to single-phase ac/ac converter for a contactless electric vehicle charger. In *2016 18th European Conference on Power Electronics and Applications (EPE'16 ECCE Europe)*, pages 1–10, 2016.

[15] N. Mohan, T.M. Undeland, and W.P. Robbins. *Power Electronics: Converters, Applications, and Design*. John Wiley & Sons, Hoboken, NJ, 3 edition, 2003.

[16] N. Mohan. *Power Electronics: A First Course*. Wiley, Hoboken, NJ, 2011.

[17] Andrzej M. Trzynadlowski. *Introduction to Modern Power Electronics*. John Wiley & Sons, Hoboken, NJ, 3 edition, 2016.

[18] J. W. Kolar, T. Friedli, J. Rodriguez, and P. W. Wheeler. Review of Three-Phase PWM AC–AC Converter Topologies. *IEEE Transactions on Industrial Electronics*, 58(11):4988–5006, 2011.

[19] T. Friedli, J. W. Kolar, J. Rodriguez, and P. W. Wheeler. Comparative Evaluation of Three-Phase AC–AC Matrix Converter and Voltage DC-Link Back-to-Back Converter Systems. *IEEE Transactions on Industrial Electronics*, 59(12):4487–4510, 2012.

[20] Robert W. Erickson and Dragan Maksimović. Pulse-width modulated rectifiers. In *Fundamentals of Power Electronics*, pages 637–701. Kluwer Academic Publishers, New York, NY, 2 edition, 2004.

[21] P. W. Wheeler, J. Rodriguez, J. C. Clare, L. Empringham, and A. Weinstein. Matrix converters: a technology review. *IEEE Transactions on Industrial Electronics*, 49(2):276–288, 2002.

[22] P. Tenti, L. Malesani, and L. Rossetto. Optimum control of N-input K-output matrix converters. *IEEE Transactions on Power Electronics*, 7(4):707–713, 1992.

[23] Jang-Hyoun Youm and Bong-Hwan Kwon. Switching technique for current-controlled AC-to-AC converters. *IEEE Transactions on Industrial Electronics*, 46(2):309–318, 1999.

[24] J. Rodriguez, M. Rivera, J. W. Kolar, and P. W. Wheeler. A Review of Control and Modulation Methods for Matrix Converters. *IEEE Transactions on Industrial Electronics*, 59(1):58–70, 2012.

[25] L. Empringham, J. W. Kolar, J. Rodriguez, P. W. Wheeler, and J. C. Clare. Technological Issues and Industrial Application of Matrix Converters: A Review. *IEEE Transactions on Industrial Electronics*, 60(10):4260–4271, 2013.

[26] Charles K. Alexander and Matthew N.O. Sadiku. *Fundamentals of Electric Circuits*. McGraw-Hill, New York, NY, 5 edition, 2003.

[27] Chwei-Sen Wang, G. A. Covic, and O. H. Stielau. Power transfer capability and bifurcation phenomena of loosely coupled inductive power transfer systems. *IEEE Transactions on Industrial Electronics*, 51(1):148–157, 2004.

[28] Chwei-Sen Wang, O. H. Stielau, and G. A. Covic. Design considerations for a contactless electric vehicle battery charger. *IEEE Transactions on Industrial Electronics*, 52(5):1308–1314, 2005.

[29] R. L. Steigerwald. A comparison of half-bridge resonant converter topologies. *IEEE Transactions on Power Electronics*, 3(2):174–182, 1988.

[30] E. L. Rees. Graphical Discussion of the Roots of a Quartic Equation. *The American Mathematical Monthly*, 29(2):51–55, 1922.

[31] K. Ogata. Mathematical modeling of control systems. In *Modern Control Engineering*, pages 13–62. Prentice Hall, Upper Saddle River, NJ, 5 edition, 2010.

[32] Eric W. Weisstein. Cubic equation. In *CRC Concise Encyclopedia of Mathematics*, pages 610–613. CRC Press, Boca Raton, FL, 2 edition, 2003.

[33] N.S. Nise. Time response. In *Control System Engineering*, pages 157–233. John Wiley & Sons, Hoboken, NJ, 6 edition, 2011.

[34] H. A. Wheeler. Simple Inductance Formulas for Radio Coils. *Proceedings of the Institute of Radio Engineers*, 16(10):1398–1400, 1928.

[35] M. Dehghanian, A. Namadmalan, and M. Saradarzadeh. Optimum design for series-series compensated inductive power transfer systems. In *2017 8th Power Electronics, Drive Systems Technologies Conference (PEDSTC)*, pages 365–370, 2017.

[36] Gyu Bum Joun and B. H. Cho. An energy transmission system for an artificial heart using leakage inductance compensation of transcutaneous transformer. *IEEE Transactions on Power Electronics*, 13(6):1013–1022, 1998.

A. Circuit Schematics

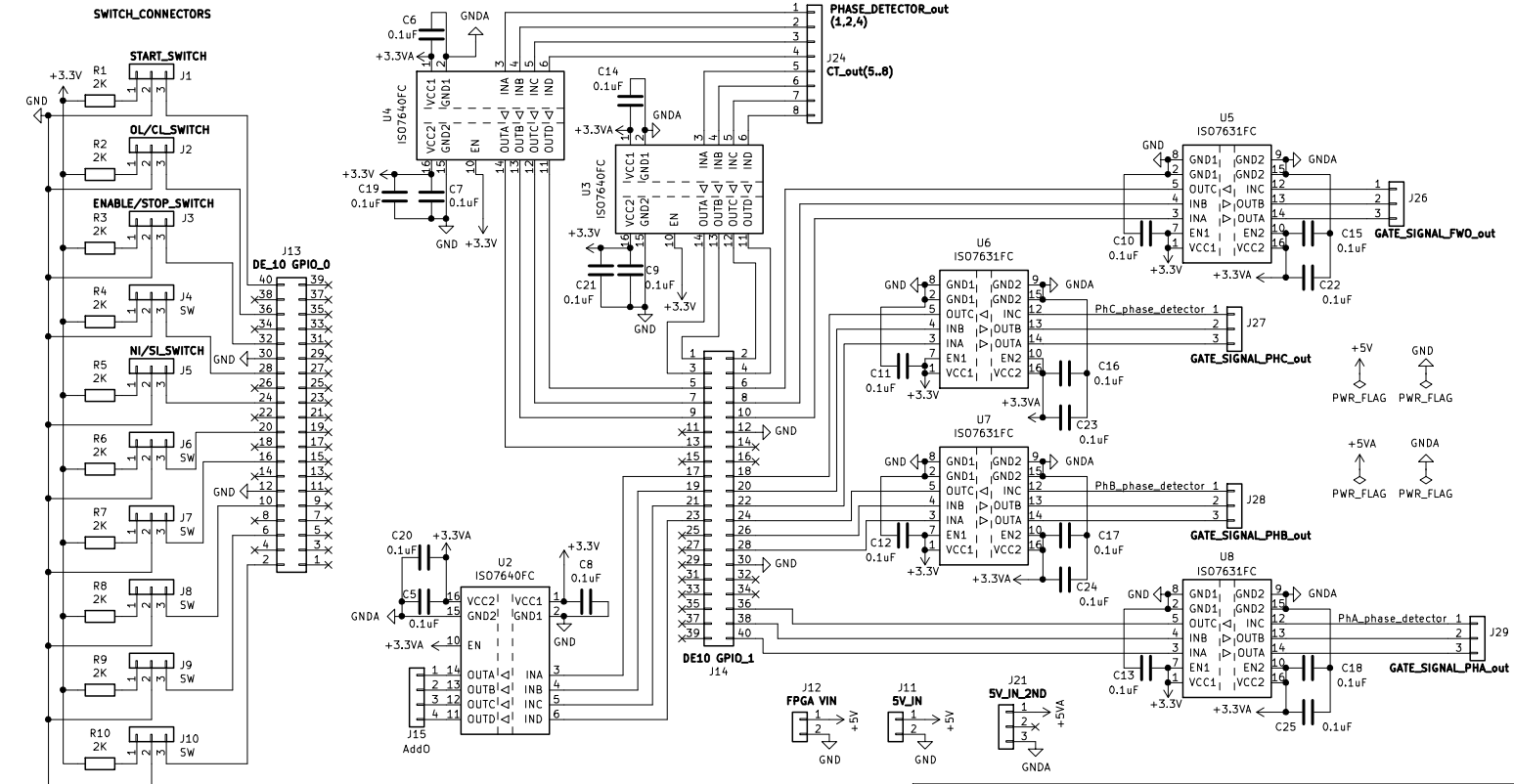

Base board for the FPGA controller. This board is connected directly to DE10-Nano, CT, PHASE-DETECTOR and four CELL boards. The PHASE-DETECTOR uses ADC-PLL, however, its schematic is not included in this book.

Designer: Ferdi Kusumah

Aalto University

Sheet: /

File: Base.sch

Title: Controller (BASE)

Size: A4	Date: 03.02.2020	Rev:
KiCad E.D.A. kicad (5.1.2)-2		Id: 1/1

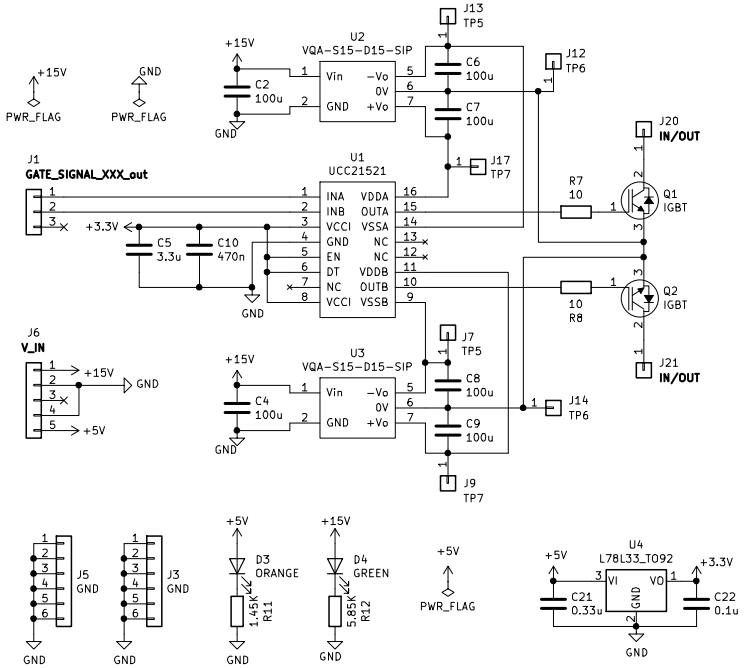

Common emitter bi-directional switch board. This board is connected directly to the BASE board. In the context of this dissertation, the common-emitter switches can be connected to either the three-phase voltage source or the free-wheeling path.

Designer: Ferdi Kusumah

Aalto University

Sheet: /

File: Cell.sch

Title: Bi-directional switch (CELL)

Size: A4	Date: 06.08.2019	**Rev:**
KiCad E.D.A. kicad (5.1.2)-2		Id: 1/1

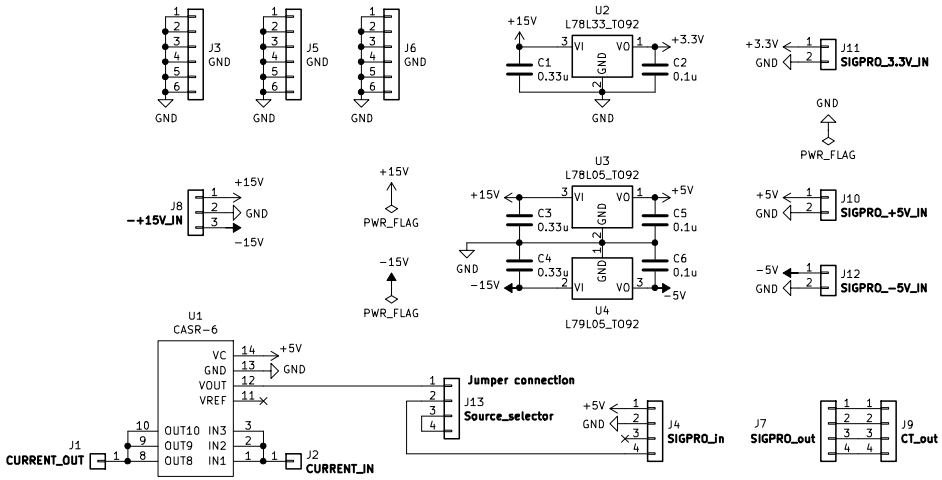

CASR−6 and Sigpro supplies board. This board is mainly used to measure current in the free−wheeling path and connected directly to the SIGPRO and BASE boards.

Designer: Ferdi Kusumah
Aalto University

Sheet: /
File: CT.sch

Title: Current transducer and power supply (CT)

Size: A4	Date: 28.06.2019	**Rev:**
KiCad E.D.A. kicad (5.1.2)−2		Id: 1/1

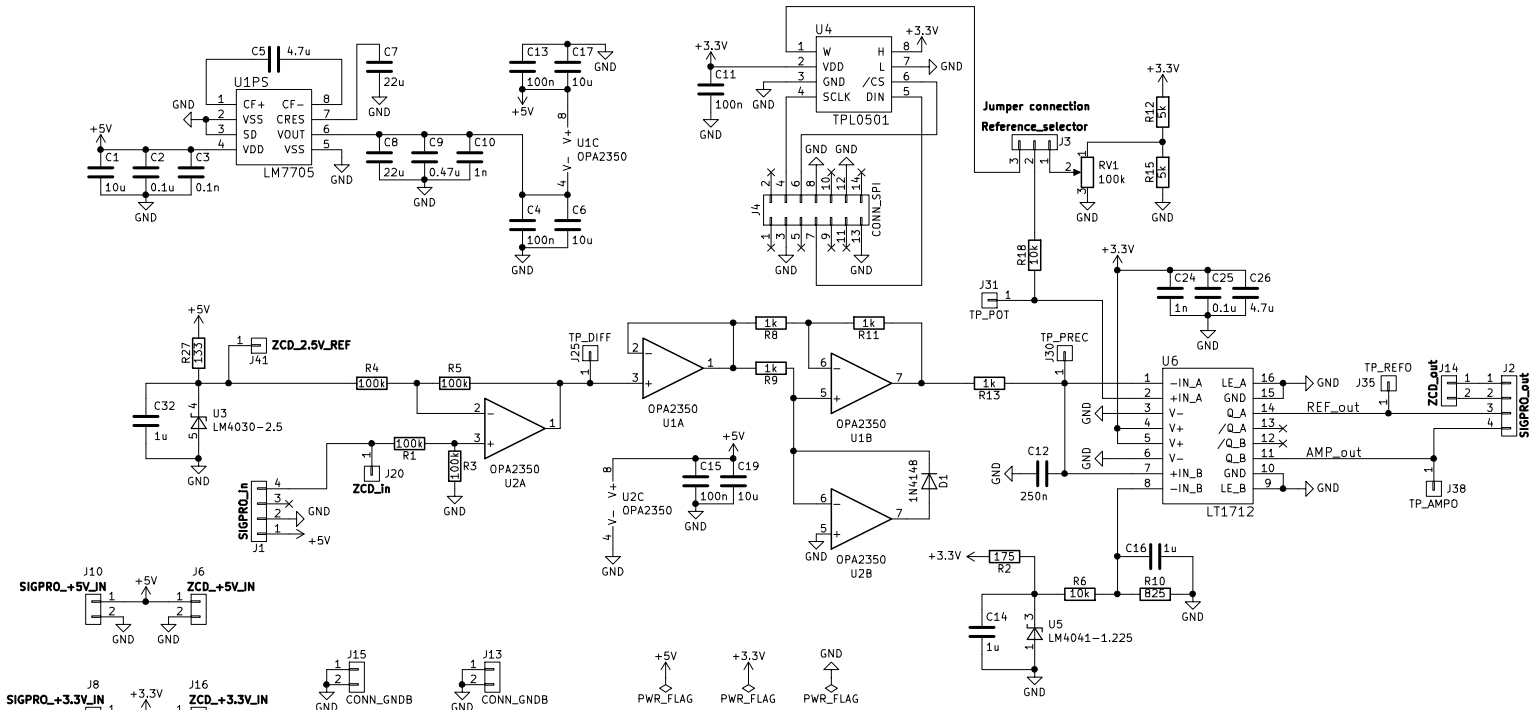

Single supply precision rectifier and voltage references board. This board is directly connected to the CT, and ZCD boards. The rectifier schematic was taken from the TI tidu024 document.

Designer: Ferdi Kusumah and Texas Instruments (TI)

Aalto University

Sheet: /

File: Sigpro.sch

Title: Signal processor (SIGPRO)

Size: A4	Date: 22.08.2018	**Rev:**
KiCad E.D.A. kicad (5.1.2)-2		Id: 1/1

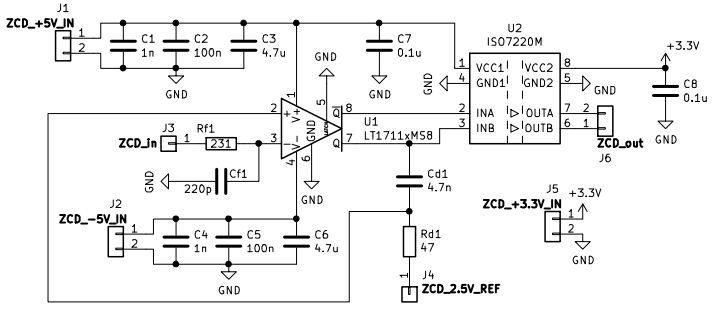

Zero-crossing detector board. This board is connected directly to the SIGPRO board.

Designer: Ferdi Kusumah
Aalto University

Sheet: /
File: ZCD.sch

Title: Zero-crossing detector (ZCD)

Size: A4	Date: 25.04.2017	**Rev:**
KiCad E.D.A. kicad (5.1.2)-2		Id: 1/1

B. FPGA Layout Flowchart

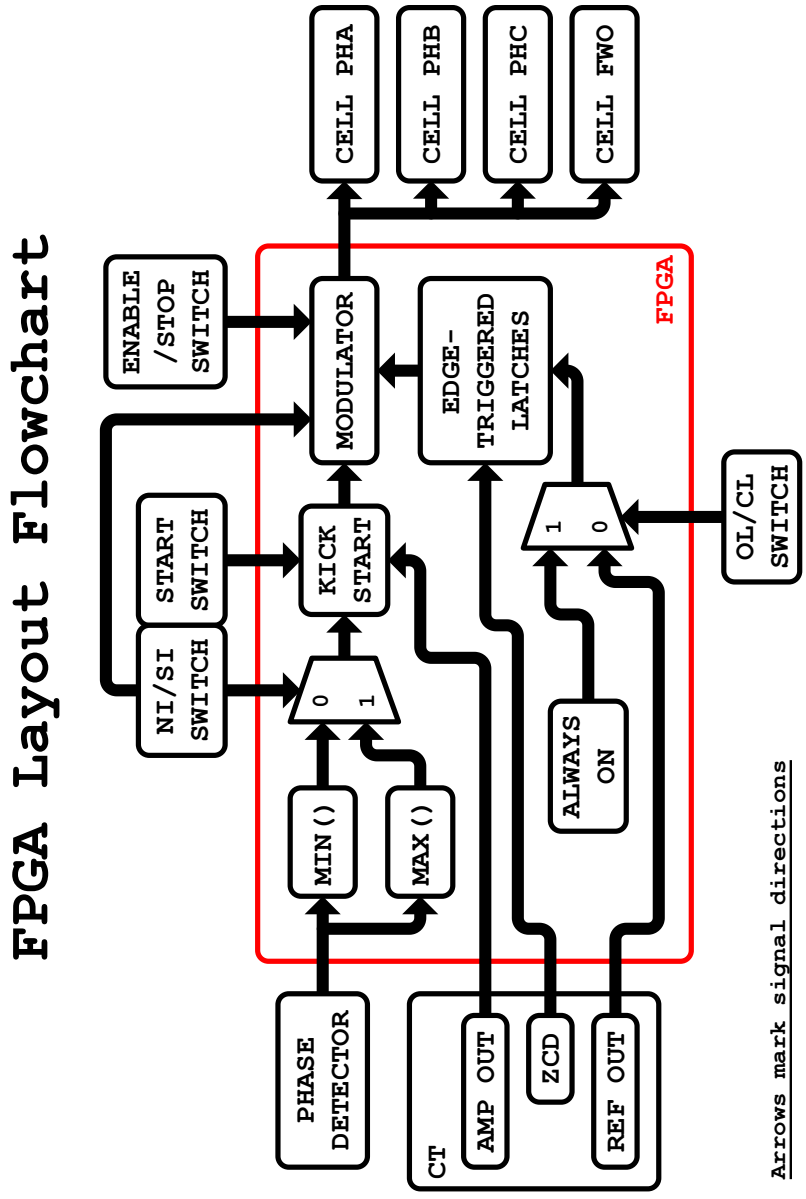

Errata

Publication I

On page 3, V_s should be

$$V_\mathrm{s} = 4V_\mathrm{A}/\pi. \tag{2.1}$$

In Equation (6), Variable A should be

$$\mathrm{A} = \frac{1}{2L_\mathrm{p}^2}\left[\frac{m^2(R_\mathrm{eq}+R_\mathrm{s})^2 - n}{1-k^2}\right]. \tag{2.2}$$

Publication III

In Equation (17), Variable $\mathbf{V_s}$ should be $\mathbf{V_{in}}$.

Publication IV

Equation (11) should be

$$\mathbf{i_p} = \frac{\mathbf{V_p}\left[R_\mathrm{s}^2 + \left(\omega_0 L_\mathrm{s} - \frac{1}{\omega_0 C_\mathrm{s}}\right)^2\right] + \mathbf{V_s}\omega_0 M\left[\mathrm{j}R_\mathrm{s} + \left(\omega_0 L_\mathrm{s} - \frac{1}{\omega_0 C_\mathrm{s}}\right)\right]}{R_\mathrm{p}\left[R_\mathrm{s}^2 + \left(\omega_0 L_\mathrm{s} - \frac{1}{\omega_0 C_\mathrm{s}}\right)^2\right] + R_\mathrm{s}\omega_0^2 M^2}. \tag{2.3}$$

Equation (12) should be

$$P = \mathrm{Re}\{\mathbf{V_p}\mathbf{i_p}^*\} = \frac{\mathbf{V_p}^2\left[R_\mathrm{s}^2 + \left(\omega_0 L_\mathrm{s} - \frac{1}{\omega_0 C_\mathrm{s}}\right)^2\right] + \mathbf{V_p}\mathbf{V_s}\omega_0 M\left[\mathrm{j}R_\mathrm{s} + \left(\omega_0 L_\mathrm{s} - \frac{1}{\omega_0 C_\mathrm{s}}\right)\right]}{R_\mathrm{p}\left[R_\mathrm{s}^2 + \left(\omega_0 L_\mathrm{s} - \frac{1}{\omega_0 C_\mathrm{s}}\right)^2\right] + R_\mathrm{s}\omega_0^2 M^2}. \tag{2.4}$$

PTS power transfer:
Variable $\mathbf{V}_s$ should be

$$\mathbf{V}_s = \frac{2\sqrt{2}}{\pi} V_o \angle -90^\circ, \tag{2.5}$$

therefore, Equation (13) is incorrect. The expression comes from an equivalent AC voltage over the secondary LC circuit.

STP power transfer:
Variable $\mathbf{V}_s$ should be

$$\mathbf{V}_s = \frac{2\sqrt{2}}{\pi} V_o \angle -193.5^\circ, \tag{2.6}$$

where the phase angle was obtained from the computer simulation.

Results:
The resonant frequency and average power of theoretical and simulation results are shown in Table 2.1. As can be seen in the table, the corrected values are closer to the simulation results than the original values. The difference of f_o between PTS and STP cases indicates the existence of the frequency split phenomenon.

Table 2.1. A comparison table between theoretical and simulation results ($k = 0.1$ and $V_o = 388.261V$)

	PTS power transfer		STP power transfer	
	f_o (kHz)	P (W)	f_o (kHz)	P (W)
Original	25.165	$15.329 \cdot 10^3$	26.52	$49.084 \cdot 10^3$
Corrected	25.165	$15.899 \cdot 10^3$	26.52	$-48.017 \cdot 10^3$
Simulation	25.192	$15.897 \cdot 10^3$	26.5	$-48.946 \cdot 10^3$

Publication V

Table 2 should be

	V_s (V_{rms})	I_p (A_{rms})	I_s (A_{rms})	P_{out} (W)
NIM	39.036	7.29	2.622	284.541
SIM	63.458	11.849	4.263	751.922

Aalto-DD 99/2021

INGREDIENTS:

AC/AC converter, bi-directional power transfer, dynamic hysteresis comparator, inductive power transfer, matrix converter, on-off control, pulse-density modulation, wireless power transfer, zero-crossing detector, zero-current switching and others, including a meme line (676=676)

ISBN 978-952-64-0453-0 (printed)
ISBN 978-952-64-0454-7 (pdf)
ISSN 1799-4934 (printed)
ISSN 1799-4942 (pdf)

Aalto University
School of Electrical Engineering
Department of Electrical Engineering and Automation
www.aalto.fi

BUSINESS + ECONOMY

ART + DESIGN + ARCHITECTURE

SCIENCE + TECHNOLOGY

CROSSOVER

DOCTORAL DISSERTATIONS